HHS Public Access

Author manuscript

Neuron. Author manuscript; available in PMC 2024 January 18.

Published in final edited form as:

Neuron. 2023 January 18; 111(2): 256–274.e10. doi:10.1016/j.neuron.2022.10.037.

Gabrb3 is required for the functional integration of pyramidal neuron subtypes in the somatosensory cortex

Rachel Babij[1,2,‡], **Camilo Ferrer**[1,‡], **Alexander Donatelle**[1], **Sam Wacks**[1], **Amanda M Buch**[1], **James E Niemeyer**[3], **Hongtao Ma**[3], **Zhe Ran S Duan**[1,2], **Robert N Fetcho**[1,2], **Alicia Che**[1,4], **Takumi Otsuka**[1], **Theodore H Schwartz**[3], **Ben S Huang**[1], **Conor Liston**[1], **Natalia V De Marco García**[1,5,*]

[1]Center for Neurogenetics, Brain and Mind Research Institute, Weill Cornell Medicine, New York, NY 10021, USA.

[2]Weill Cornell/Rockefeller/Sloan Kettering Tri-Institutional MD-PhD Program, New York, NY 10021, USA.

[3]Department of Neurological Surgery, Weill Cornell Medicine, New-York Presbyterian Hospital, New York, NY 10021, USA.

[4]Current affiliation: Department of Psychiatry, Yale School of Medicine, New Haven, CT 06519, USA.

[5]Lead Contact

Summary:

Dysfunction of gamma-aminobutyric acid (GABA)ergic circuits is strongly associated with neurodevelopmental disorders. However, it is unclear how genetic predispositions impact circuit assembly. Using *in vivo* two-photon and widefield calcium imaging in developing mice, we show that *Gabrb3,* a gene strongly associated with Autism Spectrum Disorder (ASD) and Angelman Syndrome (AS), is enriched in contralaterally-projecting pyramidal neurons and is

*Correspondence to nad2018@med.cornell.edu.

‡These authors contributed equally

Author contributions: R.B., C.F, and N.V.D designed the research. R.B. and A.D. performed calcium imaging and analysis. R.B. performed electroporations, viral injections, IHC experiments, and neuronal morphological reconstructions. C.F. and A.C. performed miniature electrophysiological recordings. C.F. performed electrophysiological recordings for intrinsic properties, optogenetics, dual injection experiments and analysis. A.M.B. and C.L. performed human fMRI and gene expression analysis. Rabies tracing experiments were performed by R.B. and Z.S.D; T.H.S., B.S.H., and C.L. designed algorithms for widefield and two-photon calcium analysis and advised on experimental design. R.B., J.E.N., and H.M. performed in vivo LFP and widefield recordings. R.B., A.D., S.W. and T.O. performed perfusions, tissue sectioning, and genotyping. C.L. and N.V.D supervised the project. N.V.D. secured funding. R.B., C.F., and N.V.D. wrote the manuscript with the help of all authors.

Declaration of interests: The authors declare no competing interests.

Supplementary Materials:
STAR Methods
References
Figures S1–S9
Tables S1–S2
Movies M1–M6

required for inhibitory function. We report that *Gabrb3* ablation leads to a developmental decrease in GABAergic synapses, increased local network synchrony and long-lasting enhancement in functional connectivity of contralateral—but not ipsilateral—pyramidal neuron subtypes. In addition, *Gabrb3* deletion leads to increased cortical response to tactile stimulation at neonatal stages. Using human transcriptomics and neuroimaging datasets from ASD subjects, we show that the spatial distribution of *GABRB3* expression correlates with atypical connectivity in these subjects. Our studies reveal a requirement for *Gabrb3* during the emergence of interhemispheric circuits for sensory processing.

eTOC Blurb

Babij, Ferrer et al. use mouse genetics and *in vivo* imaging to show that *Gabrb3* is required for the developmental decorrelation of cortical networks. *Gabrb3* removal leads to enhanced contralateral connectivity and hypersensitivity to tactile stimuli. In addition, *GABRB3* expression is spatially correlated with atypical connectivity in ASD human subjects.

Graphical Abstract

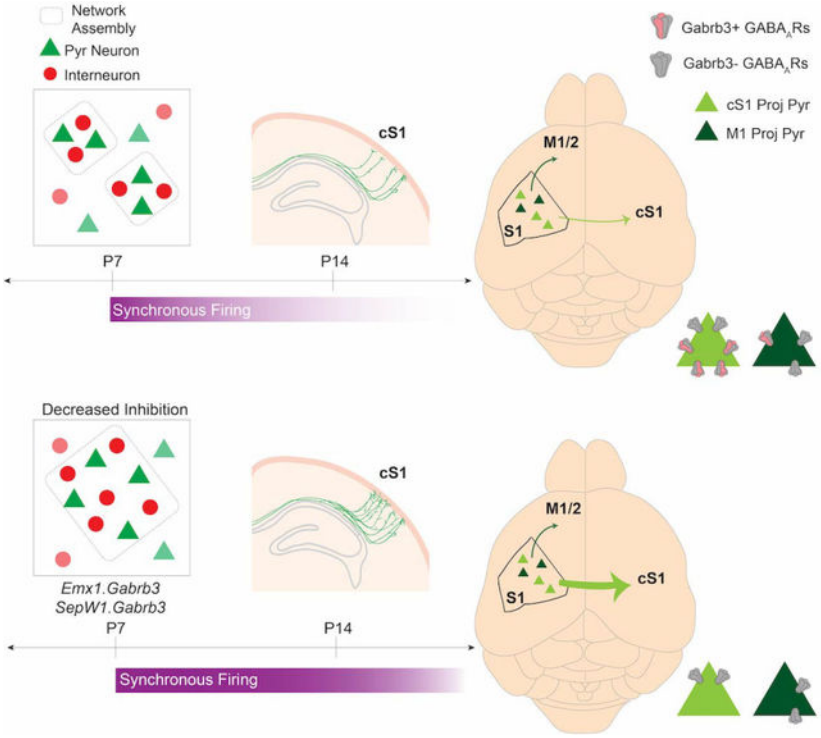

INTRODUCTION

GABAergic transmission is defective in ASD and AS [1–3]. High-risk ASD-genes involved in inhibitory synaptic function are expressed in glutamatergic projection neurons allocated to superficial cortical layers during development [4]. Among these genes is *GABRB3* which encodes the beta 3 subunit of $GABA_A$ receptor [5,6]. *Gabrb3* is expressed at high levels in excitatory neurons of the rodent and human somatosensory cortices early in development,

during a critical window for network formation, and becomes downregulated in the mature cortex, suggesting a function in early circuit assembly [7–11]. Although functional deficits in long-range connectivity are observed in ASD subjects [12,13], it is unclear if high-risk ASD genes, such as *GABRB3,* contribute to the development of cortico-cortical connections. An entry point to gain mechanistic insight is through revealing the biological function of *GABRB3* in model systems. Of particular relevance to ASD, cell type-specific manipulations are required to distinguish causative from compensatory effects.

Murine layer (L) II/III pyramidal cells (Pyr) originate in the dorsal pallium from embryonic day (E) 15 through 17 [14]. Pyr neurons can be classified based on their projection pattern, with contralaterally-projecting neurons in the primary somatosensory cortex (S1) mainly located in LII/III (>80%). These neurons extend axonal projections through the corpus callosum in a multistep developmental program involving axonal exuberance and retraction [15]. In addition to innervating contralateral targets, LII/III Pyr project to ipsilateral targets: locally to LII/III and LV as well as distally to the primary motor cortex (M1), secondary somatosensory cortex (S2), temporal association area (TeA), posterior parietal cortex (PPC) and the striatum [16,17]. Whereas extensive evidence indicates that the exuberant branching of callosal projections is activity-dependent, it is unclear how innervation patterns of specific Pyr subtypes are refined within select target areas.

Since S1 LII/III Pyr participate in network activity and receive GABAergic inputs at the time when their axons undergo substantial remodeling [18], we set out to determine the role of Gabrb3-dependent transmission in circuit refinement and stabilization. We found that *Gabrb3* is highly expressed in LII/III callosal Pyr. Developmental loss of this subunit led to decreased inhibitory function from P7 onwards in contralateral S1—but not in ipsilateral M1-projecting Pyr, resulting in tactile hypersensitivity. In addition, *Gabrb3* ablation caused a long-lasting enhancement in S1 interhemispheric -but not ipsilateral- anatomic and functional connectivity. Finally, we show that the spatial distribution of *GABRB3* expression is a strong transcriptomic predictor of atypical connectivity in ASD subjects.

RESULTS

Cortical projection neurons display a long-lasting increase in network synchronization in *Emx1.Gabrb3* mice

To determine the role of *Gabrb3* in circuit maturation, we deleted this subunit in developing Pyr by crossing $Gabrb3^{fl/fl}$ to $Emx1^{Cre}$ mice. To survey neuronal activity, we crossed them to the *Rosa.floxed.STOP.GCaMP6s* (Ai96) reporter line. These mice had normal gross brain morphology (Figure S1). To record activity patterns *in vivo*, we placed a cranial window over S1 in control ($Emx1^{Cre}$) and $Emx1^{Cre}$, $Gabrb3^{fl/fl}$ (*Emx1.Gabrb3*) mice at P6 (Figure 1A–C) and performed longitudinal two-photon calcium imaging in unanesthetized mice at P7 (Figure 1D–E, H–I, Movie 1–2), P10 (Table S1) and P14 (Figure 1F–G, J–K, Table S1, Movie 3–4). We assessed both single-cell activity, by determining individual calcium transients, as well as correlated activity, by analyzing the temporal relationship of these transients amongst the cells in the field of view (FOV). We found that event frequency increased significantly with age from P7 to P10, in both control and *Emx1.Gabrb3* mice (Table S1), likely reflecting the maturation of intrinsic electrophysiological properties of

developing pyramidal cells. However, neither the frequency nor the duration of individual calcium transients were significantly different in mutant compared to control mice at any developmental stage (Table S1), indicating that overall activity level of single cells was not affected by *Gabrb3* deletion in agreement with previously reported impact of $GABA_A$ receptor dysfunction [18].

Are Gabrb3-containing receptors required for network maturation? To address this question, we carried out Pearson's correlation analyses between cell-pairs (Figure 1). We found that control mice underwent a significant reduction in the average correlation coefficient between P7 and P14 (top panels Figure 1H–I, J–L), in agreement with the previously reported sparsification of activity using the same analysis [19,20]. In contrast, the average correlation coefficient in *Emx1.Gabrb3* mice remained elevated from P7 to P14 compared to controls (bottom panels Figure 1H–K, L). Furthermore, the correlation by distance was significantly higher in *Gabrb3* mutants both at P7 and P14 (Figure 1M–N), indicating that correlation levels are not normalized during development in mutant mice.

To characterize further the impact of *Gabrb3* loss of function on network dynamics, we determined the percentage of neuronal pairs undergoing correlated activity in the FOV, as well as the percentage of Pyr participating in network events (network participation) (Table S1, see Methods). Our analysis revealed that the percent of pairs correlated was significantly higher across development in *Emx1.Gabrb3* than in control mice (Table S1). Although network participation decreased from P10 to P14 in both control and *Emx1.Gabrb3* mice, synchronous activity remained significantly higher in the mutants (Table S1). Altogether, these data indicate that *Gabrb3* is necessary for the restriction of early correlated activity in developing LII/III pyramidal cells.

Developmental deletion of *Gabrb3* in pyramidal neurons leads to impaired GABAergic synaptic function

To establish if increased Pyr network synchrony in *Gabrb3* mutants reflects abnormal synaptic function, we characterized miniature (mIPSC) and evoked inhibitory postsynaptic currents (eIPSCs) in LII/III Pyr at P7. mIPSC recordings (Figure S2A) showed a decrease in the decay kinetics (Figure S2B–C) and unitary charge (Figure S2D) in *Emx1.Gabrb3* mice compared to controls but no changes in frequency (control: 0.23±0.03 Hz (n=9 cells) vs. *Emx1.Gabrb3*: 0.38±0.16 Hz (n=10 cells), Mann Whitney p=0.79). However, the immature state of both electrophysiological properties of LII/III pyramidal cells [21] and GABAergic synapses [22] at this stage may impair the ability to detect spontaneous neurotransmitter release in the presence of TTX. To overcome this, we assessed eIPSCs using optogenetics. We injected *AAV1.Dlx1.ChR2.mCherry* virus in control and *Emx1.Gabrb3* mice at P0 and recorded light-evoked responses at P7. To validate the approach, we performed current-clamp recordings in a subset of LII/III mCherry-expressing interneurons and recorded time-locked optogenetically-induced APs (Figure 2A). Subsequently, we recorded eIPSCs in LII/III Pyr in response to minimal light stimulation. Our analysis revealed that eIPSC amplitude was significantly reduced in mutants compared to controls (Figure 2B–C). As a complement to the electrophysiology, we quantified the density of synaptic clusters delineated presynaptically by expression of the vesicular GABA transporter (VGAT) and

postsynaptically by the scaffold for $GABA_A$ receptors, gephyrin [23] at P7 (Figure 2D). We found a significant decrease in synaptic density in *Emx1.Garbr3* compared to control mice (Figure 2E). Altogether, these results indicate that deletion of *Gabrb3* in developing Pyr leads to a decrease in GABAergic synapses during the first postnatal week.

We next determined if GABAergic dysfunction perdures through the second postnatal week in *Emx1.Gabrb3* mice. To this end, we performed mIPSC recordings in LII/III Pyr neurons at P14-P16 (Figure 2F–H). In comparison to controls, mutant mice showed a significant reduction in mIPSC frequency (Figure 2I) but not in amplitude (Figure 2J). Although a reduction in IPSC frequency could reflect presynaptic or postsynaptic defects [24], our synaptic analyses at P7 suggest that the reduction in IPSC frequency was likely caused by the postsynaptic ablation of the receptor and a reduction in the number of interneuron-Pyr synapses. In addition, the average mIPSC decay was faster in mutant mice (Figure 2H, K), resulting in reduced mIPSC unitary event charge (Figure 2L) and total inhibitory charge (Figure 2M). This result is in agreement with defective GABAergic transmission upon *Gabrb3* removal in adult Pyr [25] and likely reflects accelerated kinetics due to downregulation of the $GABA_A$ receptor alpha 2/3 subunits [26]. In contrast to the impact of *Gabrb3* removal on inhibitory drive, we found no significant differences in excitatory synaptic function (Figure S2E–L), intrinsic excitability (Figure S3A–I), dendritic development (Figure S3J–P) or lamination (Figure S4). Finally, the E/I ratio was significantly higher in mutant, compared to control mice (Figure 2N). These deficits in GABAergic transmission in *Gabrb3* mutants likely underlie the increased network synchronicity. In support of this interpretation, differences in IPSC decay can exert large changes in network synchrony in adult mice [27].

Gabrb3 is selectively required in LII/III Pyr for the restriction of correlated activity and innervation of contralateral targets

Since deletion of *Gabrb3* increases network synchrony in LII/III Pyr at P7, a stage before callosal axons branch and form synapses within target regions [14], we hypothesized that augmented synchrony could perturb axonal innervation. To test this, we analyzed axonal morphology after electroporation of a membrane-bound GFP (mGFP) construct in control and *Emx1.Gabrb3* mice (Figure 3A–B, S5A–C, Methods). Our analyses revealed an increase in cS1 innervation which was concentrated in homotypic layers in *Emx1.Gabrb3* compared to control mice at P14 (Figure 3E, F). To further assess if GABA-mediated network decorrelation is necessary for proper innervation, we analyzed axonal morphology in $Emx1^{Cre}$*::Gabrg2*$^{fl/fl}$ mice (*Emx1.Gabrg2*), in which removal of the γ2 obligatory $GABA_AR$ subunit ablates GABAergic transmission and increases correlated activity during development [18]. Similar to *Gabrb3* mutants, *Emx1.Gabrg2* mice electroporated with the *CAG-mGFP* construct (Figure 3B, right panel) showed increase axonal coverage in cS1 at P14 (Figure 3E, S5D), with significantly more arborization in superficial layers (Figure 3G) while TeA innervation was not affected (Figure S5E–F).

Because *in utero* electroporation is not restricted to a specific cortical area, we targeted S1 LII/III Pyr by injecting a Cre-dependent mGFP (*FLEX-mGFP*) virus in $SepW1^{Cre}$ and *SepW1.Gabrb3* mice at P0-P2. We subsequently analyzed axonal projections at P14-16 (Figure 3C–D, S4G–J). Similar to *Emx1.Gabrb3* mice, *SepW1.Gabrb3* mice show a

significant increase in axonal coverage (Figure 3E, H) and the percentage of axonal branches in LII/III cS1(Figure S5J). Comparable results were obtained with presynaptic *Gabrb3* deletion (Figure S5K–Q). Thus, aberrant arborization in cS1 in *Gabrb3* mutants arises from the contralateral homotypic area. To determine if *Gabrb3* deletion broadly impacts S1 efferent innervation, we analyzed projections from S1 to S2, M1/2, PPC and TeA. Our analysis revealed that projections to ipsilateral targets were not significantly different between *SepW1.Gabrb3* and control mice (Figure 3I–L).

Given the phenotypic similarities in *Emx1.Gabrb3* and *Sepw1.Gabrb3* mice, we hypothesized that aberrant cS1 innervation in the latter was also accompanied by increased correlated activity. To test this, we performed chronic imaging of Pyr in control and *SepW1.Gabrb3* mice (Figure 3 M–N, Table S2). Similar to *Emx1.Gabrb3* mice, *SepW1.Gabrb3* mutants showed an increase in the average correlation (Figure 3O–P) and the correlation coefficient over distance, compared to controls, at P7 (Figure 3Q) and P14 (Figure 3R). We found no significant differences in single cell event frequency or duration between control and mutants albeit these events became faster and shorter with age (Table S2). Together these results show that *Gabrb3* loss of function in LII/III Pyr compromises the developmental decorrelation of cortical networks and leads to exuberant axonal coverage of contralateral -but not ipsilateral-targets.

Increased contralateral anatomical connectivity upon *Gabrb3* deletion

To establish whether anatomical changes in axonal projections lead to increased synaptic connectivity, we utilized monosynaptic retrograde rabies viral tracing [28]. To target the expression of the proteins necessary for rabies infection (tumor avian virus receptor, TVA) and transsynaptic spread (B-glycoprotein, B), we performed *in utero* electroporation at E15.5 with a *pAAV-FLEX-GFP-TVA-B* plasmid in $Emx1^{Cre}$ (control) and *Emx1.Gabrb3* mice. Subsequently, we injected the same mice with fluorescently tagged rabies virus (*SAΔG-RbV-BFP* pseudocolored in red in Figure 4B–D) at P7 (Figure 4A) and analyzed presynaptic inputs at P14-P16 (Figure 4B–I, S6A–C). In this approach, starter neurons are identified by co-expression of GFP and BFP (yellow in Figure 4B–C) and presynaptic neurons by BFP expression. To determine local Pyr connectivity, we quantified the number of starters and the total number of BFP-expressing neurons in ipsilateral S1 over the total number of starter cells in S1. We found no significant differences between control and *Emx1.Gabrb3* mice (Figure 4E–F). To determine the laminar distribution of inputs, we quantified the number of BFP+ presynaptic neurons by layer per 100 starter neurons. We found that the laminar distribution of ipsilateral inputs was similar in control and *Emx1.Gabrb3* mice (Figure 4G), in agreement with the previously reported activity-independent development of LII/III S1 local collaterals [29]. In contrast, the number of contralateral Pyr per starter was higher in *Emx1.Gabrb3* compared to control mice (Figure 4H). In particular, we observed a significant increase in LII/III and LVI (Figure 4I). While interneuron density was increased in *Emx1.Gabrb3* mice (Figure S6D–H), the number of presynaptic interneurons (BFP^+) revealed by rabies tracing was not significantly different between genotypes (Figure S6B–C), suggesting that these supernumerary interneurons do not integrate in the circuit. Altogether, these results indicate that developmental deletion of *Gabrb3* leads to increased Pyr contralateral—but not ipsilateral—anatomical connectivity.

Aberrant interhemispheric functional connectivity in *Emx1.Gabrb3* mice

To determine if increased anatomical connectivity between S1-cS1 in *Emx1.Gabrb3* mice is associated with increased correlated activity across the cortical hemispheres, we performed *in vivo* widefield calcium imaging in combination with local field potential (LFP) recordings at P14 in *Emx1.GCaMP6s* (control) and *Emx1.Gabrb3.GCaMP6s* mice (Figure 5A–C) [30]. In video segments from control mice, low amplitude spontaneous activity was detected by both LFP and calcium recordings (Figure 5D, F). The calcium signal recorded from multiple locations displayed different waveforms, indicating a global desynchronization in spontaneous activity (Figure 5D). In contrast, 50% of *Emx1.Gabrb3* mice showed high amplitude global propagating activity detectable by both LFP recording and calcium imaging (Figure S7). The other half of the mutant cohort showed low amplitude activity (Figure 5E, G). We only included video segments from the latter group for further analysis. To determine overall spontaneous activity, we quantified the power and standard deviation of the LFP (s.d. LFP), and the maximum amplitude as well as the area under the curve (AUC) of the calcium signal for ROI seeds. We found that the s.d. LFP signal was significantly higher in *Emx1.Gabrb3* than in control mice, whereas the LFP power was similar between genotypes (Figure 5H, top panels). Although not significant, the amplitude of the calcium signal and AUC also showed a trend to higher values in mutants (Figure 5H, bottom panels), suggesting that *Gabrb3* deletion leads to increased cortical activity.

To determine if somatosensory pathways are differentially impacted in *Emx1.Gabrb3.GCaMP6s* mice, we used the Spearman's correlation coefficient to assess co-activation between S1 and ipsilateral or contralateral cortical regions (Figure 5I; Movie 5–6). To characterize pathway-specific differences while controlling for changes in local correlated activity within S1 (Figure 1, Table S1), we normalized long range correlation measures to local activity between two ROIs within S1 (S1–1 and S1–2) (Figure 5I–J). Our analyses revealed that correlated activity between S1 and cS1 -but not S1-M1 or S1-TeA- was significantly increased in *Emx1.Gabrb3.GCaMP6s* mice compared to controls. In addition, the correlation coefficients between S1-cM1 and S1-V1 were increased while the M1-cM1 comparison showed an increasing trend ($p=0.08$) in mutant mice compared to control. In contrast, we found that V1-cV1 correlation was not significantly different in *Emx1.Gabrb3* mice compared to controls (Figure 5J). Thus, deletion of *Gabrb3* in developing Pyr does not cause a generalized increase in interhemispheric connectivity, but rather more prominently affects sensorimotor circuits. Within these circuits, correlated activity across the S1-cS1 pathway is particularly enhanced, consistent with our anatomical results.

Gabrb3 is highly expressed in contralaterally -but not ipsilaterally- projecting pyramidal cells and is required for inhibitory synaptic function

Gabrb3 may be required for inhibitory synaptic function in Pyr with different efferent targets. To test this hypothesis, we visualized different S1 Pyr populations by means of retrograde-AAV (*AAV-rg*, Figure 6A–C) injections in regions targeted by their axons. We injected *AVV.retrograde.hSyn.mCherry* virus in ipsilateral M1 (Figure 6A, C) and *AAV.retrograde.CAG.GFP* in cS1 (Figure 6A–B) at P6-8. Subsequently, we analyzed axonal projections (Figure 6D–G) and electrophysiological properties at P13-16 (Figure 6H–O).

We found that the number of retrogradely-labeled GFP Pyr neurons in S1 normalized to the number of infected neurons in cS1 was significantly greater in *Emx1.Gabrb3* than control mice (Figure 6E); whereas the number of retrogradely-labeled mCherry Pyr neurons in S1 normalized to the number of infected neurons in M1 was unchanged between mutant and control mice (Figure 6F), in agreement with our anterograde tracing analysis (Figure 3). Further, only 2.08% and 1.58% of projecting Pyr in *Emx1.Gabrb3* and control mice respectively showed dual projections to cS1 and M1 (Figure 6G). To determine differences in the contribution of *Gabrb3* to synaptic function, we recorded mIPSCs from GFP-expressing (cS1 projecting) or mCherry-expressing (M1 projecting), but not yellow (dual projecting) Pyr (Figure 6H–O). cS1-projecting Pyr displayed a reduction in mIPSC frequency (Figure 6L) with a simultaneous acceleration of the average decay kinetics (Figure 6K, N) and no change in the amplitude of events (Figure 6M), resulting in an overall reduction of the total inhibitory charge received by cS1 Pyr upon *Gabrb3* deletion (Figure 6O). In contrast, M1 projecting Pyr displayed no significant differences in these parameters (Figure 6K–O). To determine if *Gabrb3* expression differs between cS1 and M1 projecting Pyr, we carried out RNA scope in situ hybridization with probes against *Gabrb3* in control mice previously injected with retrograde viruses (Figure 6A). Our results revealed that both cS1 and iM1 projecting neurons express *Gabrb3* at P14 (Figure 6P–Q). To quantify expression levels, we determined *Gabrb3* somatic fluorescence coverage. We found that S1 contralaterally-projecting pyramidal cells exhibit increased *Gabrb3* fluorescence coverage compared to ipsilaterally-projecting M1 neurons (Figure 6Q). Importantly, there were no significant differences in dendritic morphology between cS1 and M1-projecting Pyr in control mice (Figure S8). Thus, cS1-projecting Pyr express *Gabrb3* at higher levels than iM1-Pyr and rely heavily on this receptor subunit for GABAergic transmission during development, suggesting a cellular mechanism for the selective axonal targeting defects observed in *Emx1.Gabrb3* mice.

Increased sensory-evoked responses in neonatal Emx1.Gabrb3 mice

Cortical responses to passive whisker deflections can be detected in the somatosensory cortex from birth [31]. GABAergic signaling shapes cortical responses to these stimuli during the first postnatal week [20,32]. Therefore, we hypothesized that Gabrb3-containing $GABA_A$ receptors could be necessary in this process. To test this, we surveyed Pyr activity in un-anesthetized control and *Emx1.Gabrb3* mice in vivo at P7. To mimic perinatal interactions, we used air puffs to passively stimulate multiple whiskers applying repetitive stimulation (Figure 7A). This protocol allowed for effective displacement of all whiskers on the whisker pad and return to baseline between stimulations. We analyzed neuronal responses in a window of 5 s after stimulation and used network analysis to determine sensory-evoked network events (Figure 7B–C). Our analysis showed a significant increase in the percentage of neurons participating in sensory-evoked network events (Figure 7D), as well as an increase in the overall percentage of whisker-responsive cells in *Emx1.Gabrb3* compared to controls (Figure 7E) but no difference in the percentage of stimulations leading to evoked network events (Figure 7F). In addition, we observed an increase in the overall average pairwise correlation (Figure 7G) and correlation by distance in *Emx1.Gabrb3* compared to control mice (Figure 7H). These data indicate that developmental loss of *Gabrb3* leads to hypersensitivity to whisker stimulation as early as P7.

Regional differences in *Gabrb3* expression in humans are associated with atypical functional connectivity patterns in ASD

GABRB3 is strongly associated with ASD and AS [3,33,34]. Furthermore, fMRI studies show extensively altered connectivity patterns in humans with ASD [35]. Based on this evidence and the murine analyses, we hypothesized that *GABRB3* may contribute to ASD pathophysiology by modulating functional connectivity. To test this, we used a partial least squares regression model (PLS) to implement an unbiased evaluation of 1) whether regional differences in gene expression predict atypical connectivity patterns in ASD, and 2) the extent to which *GABRB3* and other ASD risk genes are important predictors in this model, relative to all other genes (Figures 8, S9). To quantify atypical connectivity in ASD, we performed the PLS analysis using a large-scale, publicly available fMRI datasets ABIDE1 and 2 [36,37]; see Methods, Figure S9). To rule out the effect of age on functional connectivity, we also ran the PLS model with a narrower age range during the adolescent developmental period (age 12–18) (Figure 8). We mapped normative regional gene expression profiles for 10,438 microarray probes in the Allen Human Brain Atlas Microarray (AHBA) [38,39] to the same functional parcellation. Finally, we used multivariate PLS regression to identify a linear combination of genes (PLS component) that maximizes covariation with atypical connectivity (Figure 8A), where gene weight indicates how well gene expression across cortical and subcortical parcels explains atypical connectivity. Our analyses revealed that regional differences in gene expression explained the neuroanatomical distribution of atypical connectivity in ASD by comparison with shuffled data (Figures 8B, 8D, S9A). To determine the significance of alignment between the rsfMRI atypical connectivity map and *GABRB3* expression, we compared the PLS weight of *GABRB3* with an empirical null distribution of weights for the gene (accounting for spatial correlations). This analysis revealed that the atypical connectivity map in ASD was significantly correlated with *GABRB3* expression in both the full sample and age-restricted cohorts (Figures 8C, S9B).

To assess the selectivity of the PLS analysis, we compared the ranking of a subset of previously identified high confidence genes (*GRIN2B, NRXN1, SCN2A*) to genes with limited or no association with atypical connectivity in ASD (*ACE, THRA, ACTB)* [40]. We found that *GABRB3* ranked in the top 8.2% of all negatively weighted genes, while *GRIN2B* (17.6 %), *NRXN1* (6.4%), and *SCN2A* (0.2%), were also highly ranked with strong negative weights in the PLS model (indicating anticorrelations with atypical connectivity patterns) (Figure 8E–F). In contrast, genes with limited ASD association: *ACE*, *THRA* and *ACTB* [40] ranked towards the middle of the gene list and thus were not significantly associated with atypical connectivity (Figure 8E). Further, performing the PLS analysis in the full ASD data set using a large age range (age: 5–64) converged on the results when the PLS analysis is applied to the age-restricted data set (age: 12–18) (Figures 8, S9A–D). Altogether, the mouse and human data indicate that regional differences in *GABRB3* expression are correlated with the neuroanatomical distribution of atypical connectivity in ASD and may contribute to dysfunction of select pathways as a possible mechanism of pathophysiology.

DISCUSSION

Whereas the role of neuronal activity in the development of callosal projections has long been recognized [41–43], the circuit mechanism underlying this process was unknown. We demonstrated that ablation of *Gabrb3*-containing receptors leads to GABAergic synaptic deficits as early as P7, causing abnormal co-activation of large swaths of pyramidal cells. Because interhemispheric connectivity is not observed at this stage and callosal axons do not prematurely invade the contralateral hemisphere in *Emx1.Gabrb3* mice (data not shown, [44]), this early synchronization likely begins within local circuits. At these early stages, interneuron survival is critically dependent on Pyr activity [45]and GABA-dependent regulation of network dynamics [18]. Therefore, it is not surprising that *Emx1.Gabrb3* mice display an increase in interneuron density. Despite this increase, *Gabrb3* mutants do not display exacerbated GABAergic innervation but show a reduction in GABAergic synapses, which may result from abnormal GABA-dependent synapse formation [46]. Thus, while some homeostatic responses are triggered by an increase in network synchrony in *Emx1.Gabrb3* mice, they are unable to fully compensate for decreased inhibition.

What are the consequences of increased network synchrony for the maturation of long-range connections? Although callosal development requires balanced interhemispheric activity [47], the role of inhibition in this process had not been assessed. We show that perturbation of GABAergic inputs enhances contralateral innervation and correlated activity in the second postnatal week. This excessive connectivity may arise from an increase in the number of projecting cells or axonal remodeling in *Emx1.Gabrb3* mice. Two independent pieces of experimental evidence favor the latter possibility. First, Pyr differentiation, migration and density are not significantly different in *Emx1.Gabrb3* mice compared to controls (Figure S4), suggesting that callosal Pyr are not generated in excess. Second, white matter and callosal thickness are not significantly different between genotypes (Figures S5A–C), suggesting that the number of Pyr crossing the corpus callosum is not higher in *Gabrb3* mutants. Instead, excessive synchronization across cortical hemispheres may preserve contralateral innervation through Hebbian mechanisms as described in the visual system [48].

Is *Gabrb3* widely required for the establishment of long-range connectivity? Previous studies indicate that S1 LII/III Pyr subtypes project mainly to one target and are differentially recruited during behavior [14,49,50], albeit dually projecting populations have been characterized [51]. In agreement with select projection patterns, we found that cS1 and M1-projecting neurons largely represent two independent populations. Whereas cS1 Pyr depend on *Gabrb3* for axonal maturation, M1-projecting axons may rely on other inputs or activity-independent genetic programs. Although we focused on somatosensory pathways, connectivity to other areas may be also compromised in *Gabrb3* mutant mice. Indeed, our widefield imaging suggests that functional connectivity between S1-V1 is increased in mutants. While sparse, direct [52] and indirect [53] connectivity between S1 and V1 has been described, it remains to be determined if *Gabrb3* mutants show abnormal anatomical development in these projections.

Does aberrant network correlation impact sensory processing in *Gabrb3* mutants? Developing interneurons constrain Pyr activation during sensory stimulation [20]. Our results indicate that Gabrb3-containing $GABA_A$ receptors are necessary to restrict Pyr sensory-evoked activity. Cortical *Gabrb3* deficits may contribute to the tactile hypersensitivity frequently observed in ASD [54–56]. *Gabrb3* expression is also downregulated in both Rett [57] and Fragile X syndromes [58], and mouse models for these disorders display GABAergic dysfunction [59], transient hypercorrelation in cortical networks [60] and altered sensory processing as juvenile/adults [61,62]. While assessing behavioral responses in neonatal pups is challenging, our results indicate that sensory processing defects arise as early as the first postnatal week in the mouse. More generally, increased network synchrony may be an accurate predictor of impaired behavior in neurodevelopmental disorders [63].

Does *GABRB3* dysfunction contribute to human pathology? We report that this gene is a transcriptional predictor of atypical connectivity and ranks highly among genes strongly linked to ASD (*GRIN2B*, *NRXN1*), suggesting that anatomical regions with low *GABRB3* expression are susceptible to atypical connectivity (increased or decreased) in the human brain. Although our mouse analysis suggests that hyperconnectivity in ASD subjects with *GABRB3* mutations may be limited to select contralateral homologues, some caveats make a direct comparison difficult. First, unlike the mouse connectivity phenotype, the fMRI connectivity analysis in humans was not limited to contralateral homologues and reflected general dysconnectivity (increased or decreased) in ASD individuals, not just hyperconnectivity. Second, genomic sequencing data were not available for the ASD subjects in the fMRI dataset, in contrast to the selective *Gabrb3* removal in our mouse model. Thus, genetic diversity in the human sample could influence the extent or directionality of the functional imaging phenotype. In addition, the expression data from the AHBA corresponds to adult individuals (ages 24–57) whereas the fMRI functional data sets used in our studies include younger individuals (5–64 and 12–18 years). Finally, the spatial correlation of *GABRB3* expression with atypical connectivity patterns in human ASD subjects is consistent with a contributory role of this gene, but it is also compatible with other mechanisms or genetic components. Thus, our imaging transcriptomic analyses do not conclusively demonstrate a role for *GABRB3* mutations in regulating atypical resting state functional connectivity in ASD. Instead, our work shows how *Gabrb3* disruption regulates connectivity in mice, and our imaging transcriptomic analyses provide a proof-of-principle extension of this finding to humans. Future studies in genotyped individuals with ASD could more directly test the hypothesis that *GABRB3* mutations drive specific patterns of atypical connectivity.

GABRB3 dysfunction is also associated with seizures in humans [64] and adult -but not developing- mutant mice [65,66]. Consistently, developing *Emx1.Gabrb3* mice do not display spontaneous seizures. However, a subset of these mice showed hyper-excitatory global propagation waves at P14 (Figure S7), which may lower the threshold for seizures later in life. These events in *Emx1.Gabrb3* mice were not associated with increased neuronal excitability (Figure S3A–I, Table S1), in agreement with the heterogeneity of spike rate detected during ictal/interictal events [67–69]. Thus, the high amplitude activity in *Gabrb3* mutants may reflect increased network synchronization rather than an increase in spike rate.

In summary, these results provide mechanistic insight into how genetic perturbations can manifest functionally and result in altered long-range cortical connectivity in discrete pathways in the developing brain.

STAR Methods

RESOURCE AVAILABILITY

Lead Contact—Further information and requests for resources and reagents should be directo and will be fulfilled by the lead contact, Natalia De Marco Garcia (nad2018@med.cornell.edu).

Materials Availability—This study did not generate new unique reagents.

Data and Code Availability—This paper analyzes existing, publicly available human neuroimaging data. These accession numbers for the data sets are listed in the key resources table. All other raw data reported in this paper will be shared by the lead contact upon request.

This paper does not report original code.

Any additional information required to reanalyze the data reported in this paper is available from the lead contact upon request.

EXPERIMENTAL MODEL AND SUBJECT DETAILS

Mouse Lines—All animal care and procedures were performed according to the Weill Cornell Medicine Research Animal Resource Center guidelines. Animals were housed in a controlled environment on a 12 h light/dark cycle with food and water *ad libitum*. Since synaptic $GABA_A$ receptors are heteropentameric structures containing a gamma 2 subunit, two alpha and two beta subunits [25], several mouse mutants were used to delete the beta 3 and gamma 2 subunits in maturing pyramidal neurons. All mouse lines have been described previously: *Emx1*^{Cre} (JAX 005628), *RCL-GCaMP6s* (Ai96, JAX 024106), *Gabrb3*^{fl} (JAX 008310), *Gabrg2*^{fl},(JAX 003137), *SepW1.Cre* (MGI NP-39). While the *Emx1*^{Cre} line also targets glia and Cajal-Retzius cells [75], these populations express *Gabrb3* mRNA at very low levels at late embryonic and neonatal stages [10,76]. Mice of both sexes were used for analysis. Due to the young age of the mice, the influence of sex was not analyzed. For timed pregnancies, noon on the day of the vaginal plug was counted as E0.5. Developmental age of the mice was as described in the individual experiments, ranging from P0-P16. All experiments compared genetic wild-type mice (*Cre* negative or *Gabrb3*^{WT}) to mutants (*Emx1.Gabrb3*$^{fl/fl}$, *SepW1.Gabrb3*$^{fl/fl}$, *Emx1.Gabrg2*$^{fl/fl}$). For two-photon imaging, widefield calcium imaging, axonal arborization characterization, rabies viral tracing, and lamination, controls were *Emx1*^{Cre}, as *Cre* expression was necessary for the experimental technique. For other anatomical experiments, we included both *Cre*-negative and *Cre*-positive/*Gabrb3*^{WT} mice compared with *Cre*-positive/*Gabrb3*$^{fl/fl}$ mutants. A weight deficit was noted in *Emx1.Gabrb3* mice only at P21 and 28 (Figure S1A), but did not persist into adulthood, and brain size and mass were unchanged (Figure S1B–E).

There was no significant difference in survival between *Emx1.Gabrb3* and control mice or evidence of behavioral seizures in mutant animals up to P80.

Human Imaging and Gene Expression Subjects—The human neuroimaging analyses in Figs. 8, S9 used a publicly available human dataset (ABIDE I and II) [36,37] comprising resting state functional MRI scans for N=1,031 ASD subjects and N=1,139 typically developing control subjects. See Materials and Methods, "Human Gene Expression and fMRI Analysis" for details on sample selection. We excluded 249 ASD subjects and 232 typically developing control (TC) subjects with data that did not meet quality control criteria. This resulted in all subsequent analyses including N=782 ASD subjects and N=907 TC subjects (ages 5–64), except for the analyses using a restricted age range (ages 12–18) during the adolescent development period. This restricted age range PLS analysis included 261 ASD subjects (age 12–18, N=34 females, N=227 males, mean age = 16.45, SD = 8.88) and 235 typically developing controls (ages 12–18, N=48 females, N=187 males, mean age = 16.49, SD = 8.91). Functional connectivity was computed between 247 ROI defined in an extensively validated functional parcellation [77].

For human gene expression analyses, we used publicly available data from the Allen Human Brain Atlas (AHBA), which contains brain-wide microarray samples from 3,702 brain regions distributed across the cortex, subcortex, cerebellum, and brainstem. The samples utilized in this study were collected from six neurotypical adult brains (N=6 subjects, ages 24–57, N=1/5 females/males). Structural MRI (T1) was available for all subjects with MNI sample coordinates, and RNA-seq data was available for two of the brains involving 17,609 genes sampled from 112 brain regions. After preprocessing (described in Materials and Methods, "Human Gene Expression and fMRI analysis"), there were 10,438 gene expression values for each of the microarray samples, and after assignment to the corresponding neuroimaging ROI, there was a total of 2,857 AHBA samples from the six brains assigned to 213 out of the 247 ROI.

MATERIALS AND METHODS

In Utero Electroporations—*In utero* electroporation was performed as previously described [72]. Briefly, pregnant mice were electroporated at embryonic day (E) E15.5. For rabies viral tracing of neuronal populations, a *pAAV-EF1a-FLEX-GFP-TVA-B* plasmid (Addgene, Plasmid #26197) was electroporated in *Emx1*^{Cre} or *Emx1.Gabrb3* mice at E15.5. For laminar analysis *CAG-STOP-EGFP* (generated in house) was electroporated into *Emx1*^{Cre} or *Emx1.Gabrb3* mice. For axonal targeting experiments, a *CAG-mGFP* (Addgene, plasmid #14757) was electroporated into Cre-negative or *Emx1*^{Cre} (control) and *Emx1.Gabrb3* (mutant) mice. In a separate set of experiments, a *pAAV-hSyn-FLEX-mGFP-Synaptophysin-mRuby* plasmid (Addgene #71760) was electroporated *in utero* in *Gabrb3*$^{+/+}$ or *Gabrb3*$^{fl/fl}$ mice.

Viral Injections—Injections for anterograde axonal tracing and optogenetic experiments were performed at P0-2. For anterograde tracing, an *AAV1.hSyn.mGFP-Synaptophysin-mRuby* virus (UNC Viral Core, Addgene Plasmid #71760) was injected in *SepW1*^{Cre} or *SepW1*(in which cre expression is restricted to LII/III Pyr [78]. *Gabrb3* mice, while

for optogenetics, an *AAV1.mDlx.ChR2.mCherry* (Addgene #83898) was injected in *Gabrb3*$^{fl/fl}$ or *Emx1.Gabrb3* mice; using surface landmarks for localization and post-hoc confirmation of exclusive injection to S1. For rabies tracing experiments and retrograde AAV experiments, stereotactic injections were performed at P6-P8. Modified rabies virus, *SADΔG* (SAD-deltaG_BFP (EnvA), Salk Institute), was injected in electroporated mice for the tracing of presynaptic inputs (See Rabies Viral Tracing section for more information). Precise stereotactic coordinates (P7-9: 2.5 mm anterior from lambda; 2.5 mm laterally; 400 μm deep from pia) and the volume of virus injected in each animal were kept constant. For retrograde tracing, two consecutive injections were performed, one in the motor cortex with *AVV.retrograde.hSyn.mCherry* (Addgene Plasmid #114472) and one in the contralateral somatosensory cortex with *AAV.retrograde.CAG.GFP* (Addgene Plasmid #37825) at P6-P8. We chose M1 because our axonal analysis indicated that this projection is not impacted in *Gabrb3* mutant mice (Figure 3L) and is sufficiently separated from S1 thus allowing for specific retrograde labeling of these neurons (Figure 6B–D). Reconstructions of control cS1and M1 Pyr (Figure S8A) showed no differences in dendritic morphology between the two subpopulations (Figure S8B–F).

Rabies Viral Tracing—Modified rabies viral injections on electroporated pups were carried out at P7-P8 using a Drummond Nanoject II (50 nL). After injection, pups were then returned to the dam, and perfused for immunohistochemistry analysis 1 week later. Because it takes approximately 3 days to reach high levels of viral expression, analysis at P14-P16 allowed for visualization of ipsilateral (Figure 4C) and contralateral inputs (Figure 4D) to LII/III present from P10 onwards. Processing and analysis of rabies-infected brains were performed as previously described [20,28]. In brief, consecutive 20 μm sections were collected on a cryostat (Leica CM3050S). Sections were immunostained for eGFP and were examined under a Leica M165FC fluorescent microscope for double fluorescence to identify starter neurons. All starter neurons (BFP+, GFP+) were identified and counted by region on the microscope. Representative confocal images were taken using an Olympus IX81 confocal microscope with the Fluoview FV1000 software. Results of rabies tracing experiments were quantified as the ratio of the number of inputs in a specific region divided by the number of starter cells, for the laminar quantification the data was represented as the number of inputs per 100 starter cells across layers. In agreement with our previous findings [20], the electroporation strategy allowed for sparse labeling of starter neurons (10–300 per brain), located in LII/III of S1 (Figure 4B–C). Importantly, the number of starter neurons did not differ between control and *Emx1.Gabrb3* mice (Figure 4E) and correlation analysis between the ratio of contralateral inputs per starter and the number of starter neurons showed non-significant correlation (Figure S6A), indicating that variability in the number of starter neurons across mice does not influence the outcome of the analysis. Serial sections of the S1 both ipsilateral and contralateral to rabies infected neurons were counted. For characterization of interneuron inputs, we immunostained rabies infected brains with anti-GFP, anti-Sst and Pv antibodies (see immohistochemistry section for more details). Local pyramidal neurons were identified as GFP+ cells with pyramidal morphology and the absence of Sst and Pv staining.

Immunohistochemistry—Immunohistochemistry was performed as previously described [72]. GCaMP6s- and eGFP-expressing neurons were identified by immunostaining for GFP (1:1000, Goat Anti-GFP, Rockland RL600-101-215). Identity of presynaptic partners illuminated by rabies tracing was determined by co-expression of eGFP and blue fluorescent protein (BFP) (unstained, fluorophore expressed by rabies virus). For additional classification of presynaptic partners, immunostaining was performed for MGE-derived interneuron markers: Sst (rat anti-Sst, 1:1000, Chemicon MAB354) and Pv (rabbit anti-Pv, 1:1000, Abcam ab11427). Secondary antibodies for rabies analysis were as follow Alexa488 anti-Goat (Abcam ab150129), Cy3 anti-Rat (Jackson Immunoresearch, 712-165-153) and Alexa647 anti-Rabbit (Thermofisher Scientific A-31573). For Pyr subtype analysis, neurons were filled with biocytin during whole-cell patch clamp recordings and labeled *post hoc* with streptavidin (1:1000, Streptavidin Pacific Blue, Thermo Fisher S11222). mCherry expression after AAV infection was evaluated using chick anti-RFP (1:1000, Rockland RL600-901-379). Laminar analysis was performed by staining for Ctip2 (rabbit anti-Ctip2, 1:1000, Abcam ab18465) and Satb2 (rabbit anti-Satb2, 1:1000, Abcam ab3475).

For GABAergic synapse stainings, mice were transcardially perfused with chilled PBS only. Brains were postfixed in 4% PFA for 30 minutes and immersed in a cryoprotective solution of sucrose overnight before being frozen for cryosectioning. 10-micron slices of the somatosensory barrel field (S1) were sectioned. Immunohistochemistry was performed as previously described except that primary antibodies were incubated for 48 hours rather than 24 hours. Primary antibodies were a 1:200 dilution of Guinea pig Anti-Gephyrin (Synaptic Systems #147 318) and 1:500 Anti-Vesicular GABA Transporter (VGAT) Antibody (anti-Rb) (EMD Millipore #AB5062P). Secondary antibodies were 1:500 Alexa Fluor® 488 AffiniPure Donkey Anti-Guinea Pig IgG (H+L) (Jackson ImmunoResearch #706-545-148) and 1:500 Cy™3 AffiniPure Donkey Anti-Rabbit IgG (H+L) (Jackson ImmunoResearch #711-165-152). 2–3 sections per brain in LII/III S1 were imaged at 60X, scanning 4 optical Z sections every 0.33μm (for a total of 1.2μm max projection) [23], using the same imaging conditions across sections. These images were quantified for synaptic puncta as the overlap of pre- and postsynaptic markers with the Synapse Counter plugin from ImageJ/FIJI (https://github.com/SynPuCo/SynapseCounter) following previously described methods [79]. Parameters of analysis were optimized to detect the majority of visually detected synaptic puncta and kept constant between images. Synaptic density was calculated as the number pre and postsynaptic colocalization per area unit.

The following images are composite images: Figures 1C; 3B, D, I–L; 4B–D; 6B–D; S4A, H; S5A, G, L, M, N; S6B, D, E.

RNA Scope Processing and Analysis—The protocol for RNA scope was adapted from the protocols available from ACD biosciences, Akoya biosciences, and previous work [80]. Briefly, tissue was treated according to manufacturer's instructions for the RNAScope Multiplex Fluorescent Assay (Cat # 323100, ACD, Hayward, CA). Tissue was mounted in 1x sterile PBS on charged slides and allowed to air dry overnight. Slides used in this experiment were frozen at −80 after mounting and prior to RNA scope experiments. Slides were pretreated with target retrieval buffer (Cat # 322000) for 12 min at 40°C, then treated with Protease III (Cat # 322381) for 30 min at 40°C, followed by a probe incubation

for 2 hours at 40°C. The probe used was Mm-Gabrb3 (ACD; Cat # 492441). A 3-plex positive control probe (Cat # 320881) and 3-plex negative control (Cat # 320891) were run concurrently. After probe incubation, slides underwent three amplification steps, followed by the development of horseradish peroxidase (HRP) signal fluorescence (Cat # 323110) with TSA-based fluorophore (Perkin-Elmer; TSA Plus Cyanine 5, PN #). Slides were subsequently immunostained for GFP and RFP. After allowing 15 min for the slides to air dry, slides were cover slipped in Prolong Gold Antifade Mountant (Thermo Fisher, Cat # P36930) and left to dry overnight at 4°C. Analysis of gene expression in RNA scope images was performed by analyzing single cells [81]. Cells were identified as being GFP+ (cS1-projecting), mCherry+ (M1-projecting), dual+ or dual−. Dual+ and dual− cells were excluded from this analysis. The BFP channel (RNA scope probe fluorescent) was used for analysis. Images were processed using the automatic threshold function in FIJI as used in the axonal analysis experiments. Somas were outlined and % of the cell taken up by fluorescence-positive pixels was used as an indicator of RNA expression.

Cranial Window Surgery—Surgery and imaging were performed as previously described [18,20]. Briefly, mice aged between P5-P6 were briefly anesthetized by ice-induced hypothermia for 5 min and then placed on a Snuggle Safe warmer (Lenric C21) for the remainder of the surgery. The surgical procedures were similar to previously described methods [82]. The head was scrubbed with alternating solutions of 70% ethanol and 10% povidone-iodine (Betadine). All surgical surfaces and instruments used were sterilized. Local anesthesia was provided by infiltrating bupivacaine (Marcaine 0.25%–0.5% solution) into the tissue adjacent to the intended incision lines. Scalp above the somatosensory cortex determined by stereotaxic coordinates (centered at [from Lambda]: AP 1.6–2.2, ML 1.8–2.0, DV 0.1–0.3) was removed, a custom-made, titanium head plate for small mouse pups was positioned over the area, centered around the location marked for S1 with empirically tested coordinates adjusted for the age of pups, and finally, was adhered to the skull using a veterinary adhesive (Metabond). After the head plate implantation, the mouse was placed back on ice for 2–3 min if tail-pinch reflex had returned. A craniotomy (2–3 mm in diameter) was performed at the center of the circular head plate by gently etching away the skull using the sharp edge of a sterile 16G or 18G syringe needle. After achieving hemostasis, a glass coverslip (3mm round #0, 0.1 mm, Warner instruments) was lowered on top of the brain, and warm (37C) 1% agarose was applied to the perimeter of the craniotomy to seal it. The window was then fixed to the skull using veterinary adhesives (first Vetbond, then Metabond). The pup was then placed on a heating pad with bedding for recovery for a minimum of 1 hr before returning the mouse to its home cage.

In Vivo Two-Photon Calcium Imaging—Imaging, video processing, event detection and analysis were performed as described [18]. Window implantation was performed at P6, and mice were imaged longitudinally at P7, P10-11 (labeled P10, see Table S1), and P13-16 (labeled P14). Briefly, recordings were performed on unanesthetized mouse pups of which the head was stabilized by attaching the head plate to a fixed fork positioned beneath the objective using two set screws. The pup was kept on a 37C heating pad and cotton balls or bedding were placed loosely around the animal for comfort. During imaging sessions, mouse pups spent the majority of time in a quiet resting state, interrupted by occasional limb

or tail twitches. A FluoView FVMPE-RS multiphoton imaging system (Olympus) was used for detecting brain activity in mouse pups. A Mai Tai Deepsee Ti:Saphire laser (Spectra-physics) was tuned to 920 nm for GCaMP6s excitation and the total laser power delivered to the brain was less than 60 mW. A 25X (1.05 NA) water immersion lens (Olympus) was used for imaging. *Emx1.GCaMP6s* and *SepW1.GCaMP6s* mice were imaged between 100–200 mm below pia surface. Imaging depths were adjusted as the animal matured to ensure that the same lamina was imaged across developmental stages.

For spontaneous calcium imaging experiments (Figure 1, Figure 3), image frames with a field-of-view (FOV) of 509 × 509 μm (at a resolution of 512 × 512 pixels) were scanned using a pair of galvanometer scan mirrors at a frame rate of 1 Hz for 300 frames. 2–4 FOVs were imaged per mouse during each imaging session. Each FOV was imaged to produce a single, continuous 5-minute movie. For chronic imaging, imaging sessions took place at P7, P10-11 and P13-16. For longitudinal experiments, similar FOVs were located using anatomical landmarks across developmental stages, however unequivocal tracking of the exact same group of pyramidal neurons was not performed. Mice were returned to their home cage after each imaging session. For the calcium imaging experiment with whisker stimulation (Figure 7), image frames with a field-of-view (FOV) of 509 × 509 μm (at a resolution of 512 × 512 pixels) were scanned using resonant scanning. We performed a 3-frame moving average of raw frames to remove fluorescence signal variations and obtained a final frame rate of 5 Hz for 3200 frames [83]. 1–2 non-overlaping FOVs were imaged per mouse during each imaging session. Each FOV was imaged to produce a single, continuous 10.5-minute movie.

After the last imaging session, the mice were sacrificed and the location of the cranial window was confirmed by topically placing DAPI (1:1000, Invitrogen D1306) over the window after removing the circular glass. The presence of the head plate did not appear to impair feeding, grooming, or interactions between the pup and its mother as well as littermates. Mice did not display any gross developmental impairment. We did not observe any developmental or behavioral abnormalities in any of our RCL-GCaMP6s (Ai96) mice, or mice expressing GCaMP6s from our Cre line crosses. In particular, we did not observe any pathology in *Emx1Cre.Ai96* mice used for this study or in our current large colony (n = 120 mice × 15 generations, 1800+ mice) in agreement with recent reports indicating that epileptiform activity is not observed in adult *Emx1Cre.Ai96* mice [84,85]. Consistent with the lack of GCaMP6s induced pathology, our previously published work showed that GCaMP6s-expressing cells display no signs of toxicity or developmental defects [18,20]. Furthermore, LFP recordings of control *Emx1Cre.GCaMP6s* mice did not reveal any pathological activity (Figure 5). In addition, recent evidence highlights that both virally induced and widespread expression of GCaMP6s in developing mice does not cause pathology [44,86–88]. Altogether, these observations indicate that GCaMP6s expression does not cause pathological phenotypes in *Emx1Cre.GCaMP6s* mice.

Whisker Stimulation—Whisker stimulation was performed as previously described [20], using an air puff through a 1 mm diameter tube placed anterior and perpendicular to the whiskers, approximately 1 cm away. We increased air puff duration from 100ms [20] to 500 ms to ensure stimulation of all whiskers and evoke responses more reliably. Stimulation was

gated by a solenoid valve controlled by a TTL signal from the imaging FV30S-SW software via an Arduino board (Arduino Diecimila). The pressure of the air puff was adjusted so that all whiskers on the whisker pad were displaced, but the mouse was not startled and did not display any signs of discomfort. The TTL signal was triggered every 60s to allow sufficient baseline recordings after each stimulation.

Two-Photon Image Processing—Image processing and calcium signal detection were carried out using CalciumDX software routines written in MATLAB (Mathworks) [89], available open source in GitHub repository (https://github.com/ackman678/CalciumDX). To ensure imaging data were collected from un-anaesthetized neonatal mice that are quietly resting with only cardiopulmonary or myoclonic twitch movements, videos were stabilized using a third-party algorithm (https://www.cs.cmu.edu/~kangli/code/Image_Stabilizer.html). This algorithm aligns frames based on landmarks in the videos, avoiding frame deletion. If the algorithm was unable to stabilize a video, or if the motion was excessive during the session, the entire video was discarded. Mice at P7, P10, and P14 were kept calm by being placed in bedding from the cage with the mother and littermate scent and habituated daily to the imaging apparatus from the day of the surgery to the imaging day.

Two-Photon Imaging Data Analysis—For each movie, cell contours were manually traced in the t-stack projections of the average intensity image using an edge-detection algorithm, and calcium signals were measured as the average intensity inside each cell contour [89–91]. The DF/F signal was then calculated for every contour in each frame. Calcium transients were identified using automatic detection algorithms. Briefly, baseline de-trending was performed by applying a high pass filter, and a temporal sliding window with a length of 3 frames was used to determine baseline average [92].

Data were analyzed using custom routines written in MATLAB as previously described [90]. To characterize calcium activity patterns for individual neurons, we quantified calcium transient frequency, which was measured both as inter-event interval (s) and number of events per second (mHz) for each cell as well as duration, which was measured as the time between onset and offset of a calcium event. The frequency and duration were measured for each cell (or ROI), then averaged for all the cells in one movie. To identify significant correlation between any two cells within a recording, the onset of each event was represented by a Gaussian (±1 frame), and distance correlation values were calculated. Given the prolonged silent periods we observed typical in developing neuronal networks (Pyr single-cell inter-event interval of ~60–70 s), this method is an appropriate method for quantifying synchronous calcium activity at this stage. The significance of the correlation was determined via Monte Carlo simulation and the percentage of cell pairs significantly correlated were reported for each recording. A pair of cells was deemed significantly correlated when the correlation coefficient of the experimental data exceeded the $p < 0.01$ threshold from a distribution of correlation values from 1000 randomly shuffled event data sets. Correlograms were constructed by plotting lines between all cells determined significantly correlated as described above with color representing the magnitude of the Pearson's correlation coefficient between cell pairs. Average correlation and correlation coefficient by distance were calculated as the mean Pearson's correlation coefficient

between all cell pairs or between each cell pair within a determined distance threshold, respectively. Synchronicity of network activity was quantified as previously described [19,90]. Statistical significance for network events was determined via Monte Carlo simulation. The time points where the percentage of cells active exceeded or dropped under the threshold were set to be respectively the onset and offset of network events. These time points were used to quantify the duration of network events. The magnitude of network events was quantified as the peak percentage of cells coactive in each network event and was averaged for all events across a movie. The number and magnitude of network events was quantified for each movie. To determine network events, the percentage of neurons that must be simultaneously co-active to represent a statistically significant event was calculated using surrogate activity histograms by reshuffling recorded events in each neuron 1000 times to create a distribution of event sizes. Network events were defined as events with more cells active than the 99th percentile of the overall event distribution ($p < 0.01$). Note that combinatorial analyses, both network and pairs correlated, are independent of differences in the number of cells per FOV. For whisker stimulation experiments, network events were identified as described above, and events with an onset time within 5 s after the offset of air puff were deemed as evoked by stimulation. The percent of responsive cells during this window and the number and magnitude of evoked significant network events were quantified for each movie. Statistical analyses were performed on the mean of all movies from multiple animals for each genotype, treatment group, and developmental stage. If more than one movie from the same mouse were used for a given age, these movies corresponded to non-overlapping FOVs and therefore consisted of different cell populations.

Electrophysiology—Whole-cell patch-clamp recordings were performed on layer II/III pyramidal neurons in acute brain slices in the barrel cortex, as previously described [18] Both female and male mice (P8-9/ P13-16) were deeply anesthetized using isoflurane and then decapitated. Brains were rapidly removed and immersed in ice-cold oxygenated (95% O2 and 5% CO2) dissection buffer containing (in mM): 83 NaCl, 2.5 KCl, 1 NaH2PO4, 26.2 NaHCO3, 22 Glucose, 72 Sucrose, 0.5 CaCl2, and 3.3 MgSO4. Coronal slices (300 μm) were cut using a vibratome (VT1200S, Leica) and incubated in dissection buffer for 40 min at 34°C. Slices were stored at room temperature for reminder of the recording day. All slice recordings were performed at 34°C. Slices were visualized using IR differential interference microscopy (DIC) (BX51WI, Olympus) and a CMOS camera (ORCA-Flash4.0 LT, Hamamatsu). The barrel cortex was visualized and identified using a 10X Olympus objective (0.3 NA), and individual cells were visualized and targeted using a 60x Olympus water immersion (1.0 NA) objective. In most experiments, pyramidal neurons were targeted for recordings based on their typical pyramidal morphology, exhibiting a clear apical dendrite. For all recordings, external buffer was oxygenated (95% O2 and 5% CO2) and contained (in mM): 125 NaCl, 25 NaHCO3, 1.25 NaH2PO4, 3 KCl, 25 dextrose, 1 MgCl2, and 2 CaCl2. Patch pipettes were fabricated from borosilicate glass (OD 1.5/ID 0.86, Sutter Instrument) to a measured tip resistance of 3–6 MΩ. Signals were amplified with a Multiclamp 700A amplifier (Molecular Devices), digitized with an ITC-18 digitizer (HEKA Instruments Inc.) and filtered at 2 KHz. Data were monitored, acquired and analyzed using Axograph software. Series resistance was monitored throughout the experiments by applying a small test voltage step and measuring the capacitive current. Series resistance was

10~25 MΩ and only cells with <20% change in series resistance and holding current were included for analysis. Liquid junction potential was not corrected.

For experiments measuring mIPSCs and mEPSCs, pipettes were filled with an internal solution containing (in mM): 125 CsMeSO4, 10 TEACl, 10 HEPES, 0.1 EGTA, 4 Mg-ATP, 0.3 Na-GTP, 10 phosphocreatine, 0.3% biocytin, adjusted to pH 7.3 with CsOH and to 278 mOsm with double-distilled H2O. The extracellular solution also contained Tetrodotoxin citrate (1μM, Abcam) to block spontaneous firing. Recordings began at least 5 min after initial whole-cell patch was achieved to allow dialysis of the internal solution. mEPSCs were recorded holding the membrane potential at −60mV and mIPSCs were recorded at 0mV (the reversal potential for glutamatergic currents under our recording conditions). For both mEPSCS and mIPSCs the baseline was recorded continuously for 5 mins. Current segments with excessive noise or unstable recordings were excluded from analysis and discarded. Recorded traces were digitally filtered at 1kHz, the baseline was subtracted and miniature synaptic events were analyzed using template matching in Axograph X. Average amplitude and frequency of synaptic events were calculated in each cell. Decay was calculated fitting a single exponential function to the decay phase of the averaged mEPSC or mIPSC in each recorded neuron and expressed as the time constant of the fitted function. Unitary charge was calculated as the average integral of individual detected events and total charge as the added charge of individual synaptic events over a five-minute period. E/I ratio was calculated as the total charge ratio of mEPSCs and mIPSCs in the same cell over a five-minute period. For rAAV experiments, GFP+ (cS1 projecting) and mCherry+ (M1 projecting) cells were selectively targeted for recording. The observed phenotype on mIPSCs recorded from the cS1-projecting population (Figure 6) was consistent with the overall Pyr population (Figure 2). Since callosally-projecting neurons are predominantly located in LII/III [14,15], our blind patching experiments likely contain more cS1 than M1 projection neurons due to the abundance of the former in these layers (Figure 2F–N). The average number of cS1 projecting Pyr/# cells infected at the injection site was 0.06±0.01 (n=4 control mice) whereas this number was 0.03±0.01 (n=4 control mice) for M1 projecting Pyr (2:1 ratio) (Figure 6D–F).

For current clamp experiments, pipettes were filled with an internal solution containing (in mM): 125 potassium gluconate, 10 KCl, 10 HEPES, 4 Mg-ATP, 0.3 Na-GTP, 0.1 EGTA, 10 phosphocreatine, 0.3% biocytin, adjusted to pH 7.3 with KOH and to 278 mOsm with double-distilled H2O. Resting membrane potential (RMP) was measured within the first minute of breaking in. For all other measurements, RMPs were held between −60 to −65mV. Current pulses of 500 ms duration were used for stimulation, starting from −50 pA and subsequent +10pA increments until reaching maximal firing. Action potential (AP) threshold was measured at 15 mV/ms. Input resistance was measured using the slope of the I-V curve during hyperpolarizing current steps. Adaptation ratio was measured as the ratio of the first inter-spike intervals (ISI) over the average of the last 2 ISI during maximal firing frequency. Data analysis was performed using Axograph built-in analysis and IGOR Pro software (Wavemetrics).

Optogenetic Stimulation—*AAV1.Dlx1.ChR2.mCherry* injected mice at P0, were sectioned at P7-9 and recordings were targeted to the site of infection in S1 identified

by mCherry expression. Minimal evoked IPSCs in LII/III pyramidal cells were recorded in voltage-clamp configuration at a holding potential of 0mV (using the Cs-based intracellular solution). Blue light stimulation was directed locally in LII/III at 60X magnification and the stimulation adjusted to achieve at least 20% failure rate (2ms, 0.2–1% LED power), using a Mightex LED arm attachment. Responses were averaged from (8–10) individual traces of repetitive stimulation (delivered every 20 s) with the same onset response across trials, containing only one clear response in a 20ms window after stimulation and excluding failures. Peak amplitude was quantified for each cell from the averaged evoked minimal IPSC.

Dendritic Morphological Reconstruction—Morphological analysis was carried out as previously described [72]. Following the recording session, pipettes were retracted and slices were post-fixed in 4% PFA for 24 hours. Washed in PBS and treated with fluorescence conjugated streptavidin (1:500) overnight at 4°C, washed again in PBS and mounted. Stained sections were imaged in a confocal microscope (Olympus IX81). The area imaged consisted of a 3X3 array of 60X individual images, at 1um steps from the surface of the slice and encompassing all stained tissue. Post-hoc morphological analysis of pyramidal neurons was done including biocytin in the recording pipette and staining with fluorescence conjugated streptavidin (1:1000). Dendritic trees were reconstructed on Neurolucida (MBF Bioscience) for process length, number of bifurcations, number of ends, and number of nodes. Scholl analysis was performed using 30 um steps in Neurolucida Explorer.

Lamination Analysis—After immunostaining, stereological sections of S1 were imaged as previously described [18], taking 5 evenly spaced sections from within the somatosensory barrel field. Lamina was identified by DAPI staining, and cell bodies were classified according to the laminar location of soma. The soma position was expressed as distance from pia/full cortical thickness and averaged for all cells in a mouse.

Previous evidence has shown that pyramidal cell activity regulates interneuron survival [18,45]. To determine if *Gabrb3* deletion leads to increased survival, the density of somatostatin (Sst)- and parvalbumin (Pv)-positive interneurons was quantified at P14 (Figure S6D–E). Our results revealed that the density of interneurons derived from the medial ganglionic eminence (the sum of Sst and Pv interneurons) was significantly increased in *Emx1.Gabrb3* compared to control mice (Figure S6F). Pv interneuron density was increased in LII/III and V (Figure S6G), whereas Sst interneuron density was higher in LIV, V, and VI (Figure S6H). These results indicate that *Gabrb3* removal in Pyr leads to a compensatory increase in interneuron survival. To assess changes in interneuron to Pyr connectivity, in a subset of rabies tracing experiments (presented in Figure 4), the number of Sst and Pv interneurons presynaptic to starter Pyr in ipsilateral S1 was quantified. We found that the total number of presynaptic interneurons was not different in mutants compared to controls (Figure S6B–C). These results, in combination with the decrease in GABAergic synaptic function both at P7 and P14 in *Emx1.Gabrb3* mice (Figure 2C, I), suggest that supernumerary interneurons are not properly integrated in the circuit in *Gabrb3* mutant mice.

Axonal Imaging Analysis—We analyzed axonal morphology using a myristoylated GFP (mGFP) construct. To target LII/III contralateral Pyr, control and *Emx1.Gabrb3* mice

were electroporated with a *CAG-mGFP* construct at E15.5, a stage when most of these cortical projection neurons are generated [93] and axonal projections were analyzed at P14-16 (Figure 3A–B), when long-range axons have undergone elaboration in the contralateral somatosensory cortex. Neither the thickness of the white matter nor that of the corpus callosum were significantly different in mutants and controls (Figure S5A–C). Stereological sections of S1 were imaged as previously described [18], taking 5 evenly spaced sections from within the somatosensory barrel field on both sides (hemispheres) of the brain. Regions of interest were identified using the Developmental Brain Atlas [94] and the Allen Brain Atlas [11]. For experiments using non-conditional expression of *mGFP*, electroporated neurons were counted within stereologic sections of S1. Axonal images were thresholded using ImageJ built-in software, default thresholding method enabling quantification of the total number of white (axonal) and black (non-axon) pixels. For analysis within contralateral S1, each lamina was analyzed separately and defined by DAPI staining. Axonal coverage was computed as # of white pixels / # total pixels in a given area and normalized to the number of total infected/electroprated cells. Distribution of axons was computed for each section individually as # white pixels in a given layer / # white pixels in entire section, and then averaged across all sections for a given mouse. Axonal coverage in ipsilateral targets was analyzed for total coverage as in contralateral S1 and normalized to the total number of infected neurons. Similar analyses were performed after viral infection with *pAAV-hSyn-FLEX-mGFP-Synaptophysin-mRuby.* To determine if enhanced innervation is more prominent in certain laminae, we quantified the axonal coverage within each lamina defined by DAPI. For this set of experiments, we restricted our analysis to brains in which >90% infected neuronal somata were located in S1 and off-target expression was not observed in neighboring areas including S2 (Figure S5G, I).

To determine if Gabrb3-containing receptors are required presynaptically in callosal Pyr, these cells were sparsely targeted with electroporation (*FLEXm-GFP*) at E15.5 and subsequently injected *AAVSynCre* control in *Gabrb3*$^{fl/fl}$ mice at P0 (Figure S5K–M). We observed a significant increase in the percentage of axons allocated to superficial layers in cS1 in mutants compared to controls at P14 (Figure S5N–Q), similar to the pattern of distribution in other models (*Emx1.Gabrg2,* Figure S5D; *SepW1.Gabrb3*, Figure S5J). Furthermore, these axonal defects cannot be explained by abnormal neuronal differentiation, survival or migration as these processes proceeded normally in *Emx1.Gabrb3* mutants (Figure S4). In addition, the total number of infected cells with *AAV-hSyn-FLEX-mGFP-Synaptophysin-mRuby* (Figure S5H) or *AAVSynCre* (Figure S5O–P) was not significantly different between control and mutant mice.

Widefield and LFP Imaging and Analysis—Concomitant calcium imaging and LFP recordings were performed (Figure 5D–G), allowing visualization of neuronal activity across distant cortical regions including the somatosensory, motor, visual and association cortices [86,87]. All mice were anesthetized with isoflurane in 70% N_2: 30% O_2, 5% induction, and 1–2% maintenance for the imaging window implantation. Body temperature was maintained at 37°C with a regulated heating blanket (Harvard Apparatus). The head was fixed in a stereotaxic apparatus [95–97]. The skin and soft tissue over the head were carefully removed to expose an area > 8 mm in diameter. A head plate with an 8 mm opening was mounted

over the skull with dental cement. A small hole was carefully drilled over the right S1 for LFP recording. The mice were then allowed to recover for 30 minutes and then transferred to the imaging chamber. The head plate was fixed to a clamp to immobilize the head. The mouse was placed on an air floated chamber, allowing the mouse to ambulate while head-fixed within the chamber. The widefield calcium recording videos were devoid of movement artifacts as the mice are head restrained and able to artificially ambulate on a floating chamber (see[98]). The local field potential (LFP) was recorded with a glass microelectrode (50–100μm tip opening) filled with 0.9% NaCl saline. The microelectrode was carefully placed in the right S1, using whisker stimulation as a reference (Figure 5B), and implanted in close apposition to this region (~300 μm below the cortical surface). The LFP was amplified (1000x) and band-pass filtered (1–500 Hz) using an A-M systems amplifier (Model 1800, Sequin, WA, USA), digitized via CED Power 1401, and recorded by a computer running Spike2 software (Cambridge Electronic Design, Cambridge, UK). A "temporal separation" technique was employed to simultaneously image wide-field calcium and a IOS [30]. A CCD camera (J-MC023MGSY, Lighting Mind Inc., Changchun, China) using a tandem lens (85 mm × 50 mm) arrangement was focused 300–400 μm below the cortical surface. Two LEDs with coupled bandpass filters were employed as the illumination source, including a "blue" LED (470 ± 10 nm) for calcium imaging and a "green" LED (530 ± 10 nm) for IOS imaging. The illumination was directed to the cortex using optical fibers. A 510 nm long-pass filter was placed before the camera. The multispectral switching among the two LEDs was time-locked to camera frames using an Arduino board. The calcium imaging was performed every odd frame and green IOS was performed every even frame. The camera was sampling at 40 Hz, resulting in a 20 Hz imaging for calcium and green IOS, respectively. For widefield imaging, we analyzed 5000-frame segments of video. The total LFP power was calculated during 5 min recording window (power = Σf(t)^2), and computed the standard deviation of the LFP power. For the calcium data, the maximal amplitude and area under the calcium curve were also computed.

Data Analysis for Widefield Imaging—Custom-written software in MATLAB 2018A was used for data processing and statistical analysis of 5000-frame segments of video. The correlation of activity among cortical areas was assessed by placing ipsilateral and contralateral region of interest (ROI) seeds in S1, M1, TeA and primary visual cortex (V1) (Figure 5C). Correlation among different regions was normalized by dividing correlation coefficients between regions by the intra-S1 correlation coefficient. The pulsation artifact from the heartbeat was eliminated with an offline algorithm [30]. Briefly, an average QRS interval was obtained for each pixel in each trial. The peaks of R waves were obtained from ECG. An averaged pulsation artifact was obtained by an R wave-triggered average. This averaged pulsation artifact was repeatedly subtracted from each heartbeat cycle of the original data. In order to increase the signal-to-noise ratio, imaging data were convolved with a spatial Gaussian kernel (σ = 3 pixels). For calcium signal processing, the functional hemodynamic artifact was separated using the following equation [99,100]:FTrue(t)/FTrue(t0) = [F(t)/F(t0)]/[I(t)/I(t0)] where FTrue is the calcium fluoresce intensity absenting hemodynamic artifact, F is the recorded calcium fluorescence intensity, I is the recorded IOS signal at 530 nm, and t0 is the time point for baseline. The baseline fluorescence was the 5th percentile of the maximal fluorescence intensity. Note that although we did apply the

hemodynamic correction, neural activity at early postnatal stages does not evoke significant blood flow increases [101]. Thus, the functional hemodynamic artifact is likely to be minimal in the somatosensory cortex during the first 2 postnatal weeks.

Human Gene Expression and fMRI Analysis—The analyses in Figs. 8, S9 used a publicly available human neuroimaging dataset (ABIDE I and II) [36,37] comprising resting state functional MRI scans for N=1,031 ASD subjects and N=1,139 typically developing control subjects. We used standard preprocessing steps including spatial filtering, temporal bandpass filtering (0.01–0.1 Hz), motion correction, and nuisance signal regression for removal of nuisance signals related to head motion, physiological variables, and local and global hardware artifacts [102–104]. Preprocessing code is available from the corresponding author. Subjects were excluded from all subsequent analyses if they did not have at least 180s time remaining following fMRI scan preprocessing with motion censoring and had voxels with TSNR<75 in all 247 Power ROI used in the study. Motion censoring excluded frames with greater than 0.3mm of frame-wise displacement, measured by the Euclidean norm. After excluding 249 ASD subjects and 232 typically developing control (TC) subjects with data that did not meet these quality control criteria, all subsequent analyses involved N=782 ASD (99/683 females/males) subjects and N=907 (219/688 females/males) typically developing control (TC) subjects. We applied an extensively validated 247-region functional parcellation of the human brain [77] to the fMRI data, and generated whole-brain functional connectivity matrices for each participant, as measured by interregional correlations in spontaneous fluctuations in the fMRI BOLD signal between each ROI and every other ROI. To map the spatial distribution of functional connectivity differences in ASD, we tested for differences in ASD individuals vs. typically developing controls, yielding a 247-by-247 element Z-scored connectivity matrix. To minimize overfitting by reducing the dimensionality of the connectivity matrices, we summed across all statistically significantly different connections for each ROI, yielding a single atypical connectivity Z score for each brain region (Figure 8D). Because atypical connectivity patterns in ASD involve both weakened and strengthened connections in various networks [35,105–110], we designed our analysis agnostic to the directionality of connectivity differences. We quantified atypical connectivity using Welch's t-test to compare functional connectivity in ASD subjects and TC subjects.

Next, we generated a matrix quantifying gene expression in the same functional ROI, using the Allen Human Brain Atlas (AHBA), which contains brain-wide microarray samples from 3,702 brain regions distributed across the cortex, subcortex, cerebellum, and brainstem. The samples were collected from six neurotypical adult brains (ages 24–57, n=1/5 females/males). Structural MRI (T1) is available for all subjects with MNI sample coordinates, and RNA-seq data (used for preprocessing and quality control as noted below) is available for two of the brains involving 17,609 genes sampled from 112 brain regions. Preprocessing of microarray data consisted of two steps: 1) probe to gene assignment and 2) anatomical sample location to functional ROI assignment, and we followed the guidelines outlined in [111] for both steps. For step 1, we (a) reannotated probes to include updated Entrez ID assignments, (b) filtered out microarray probe expression that did not exceed background levels (due to non-specific hybridization), (c) measured the correspondence

between microarray probe expression data and RNA-seq gene expression, (d) selected one probe per gene as the probe whose regional expression most corresponded with the RNA-seq expression with a threshold of at least 0.2 correlation (thus removing genes to which a probe was not mapped or that did not meet the threshold), and (e) standardizing all gene symbols to the Hugo Gene Nomenclature Committee (HGNC) nomenclature. This resulted in 10,438 gene expression values for each of the microarray samples. *For step 2*, in each AHBA subject, we assigned the microarray samples to the 247 functional ROI by (a) assigning microarray samples and functional ROI to major anatomical parcels (cortex, subcortex, cerebellum, and brainstem), (b) in each anatomical parcel measuring the Euclidean distance from the MRI coordinates of each microarray sample in the parcel to the centroid of each functional atlas ROI in that parcel, (c) assigning each microarray sample to the closest functional ROI within 5 mm, and (d) averaging the gene expression value in each functional ROI across all assigned microarray samples for each gene. This resulted in 2,857 AHBA samples from the six brains assigned to 213 out of the 247 ROI. Following assignment, gene expression was standardized by the z score of the $\log_2$ of each value.

To investigate whether brain-wide gene expression predicts ASD-related changes in resting state functional connectivity, we utilized partial least-squares (PLS) regression using the SIMPLS algorithm (Matlab *plsregress*) with the 213 brain regions as samples, the 10,438 gene expression values across these samples as predictors (X), and atypical connectivity as the response variable (Y). Atypical connectivity was calculated for each ROI as the sum of positive atypical connectivity minus the sum of negative atypical connectivity to each Power ROI. The resulting PLS model outputs gene expression coefficients corresponding to the weight for each gene in X, which represents how much each gene contributes to the PLS component score of gene expression predicting atypical connectivity in ASD.

To increase the robustness of the analysis, we bootstrapped the gene weights in 1,000 bootstraps with replacement and ranked the genes by the gene weight divided by the standard error of its bootstrap distribution. Statistical significance of the resulting PLS model was evaluated using a spatially aware permutation test [112], which preserves the native correlation structure of gene expression across the cortical surface, as well as a commonly used random permutation test. We also repeated our PLS analysis described above in a restricted age sample (ages 12–18). We chose this age range as it represents a restricted age range early in life, it includes the adolescence period of development in humans and there were an adequate number of subjects in the ABIDE sample to allow us to perform the PLS regression analysis. We used 100 bootstraps for the PLS model since calculating the null distribution for the bootstrapped *GABRB3* gene weight requires running the PLS model 1,000 × 100 times to calculate the null distribution and using 1,000 bootstraps (which would require running 1,000 × 1,000 PLS models) was computationally infeasible (Figures 8C and S9B). This restricted age range PLS analysis included 261 ASD subjects (age 12–18, n=34 females, n=227 males, mean age = 16.45, SD = 8.88) and 235 typically developing controls (ages 12–18, n=48 females, n=187 males, mean age = 16.49, SD = 8.91) for calculating atypical connectivity. Bootstrapped gene weights were calculated as the gene weight divided by the standard error of its bootstrap distribution. To assess significance of the association of *GABRB3* expression patterns with atypical connectivity, we compared the bootstrapped PLS

gene weight for *GABRB3* (bootstrapped 100 times) with the corresponding null distribution of bootstrapped *GABRB3* gene weight from the 1,000 spins.

Previous human analyses have identified co-expression of ASD genes in specific cortical regions associated with ASD pathology. To understand the relative importance of *GABRB3* expression to atypical connectivity in ASD, we compared expression patterns of co-variation of *GABRB3* with a previously identified subset of genes that confer different degrees of ASD risk [40]. To that end, we generated a correlation matrix depicting the similarity of the transcriptional profiles for these genes. We found that *GABRB3* was co-expressed with other high risk-ASD genes including *GRIN2B*, *NRXN1* and *SCN2A*, which were also highly negatively weighted in the PLS analysis (Figure S9D–F), suggesting that downregulation in the expression of this set of genes may underlie atypical connectivity in select brain areas.

QUANTIFICATION AND STATISTICAL ANALYSES

Statistics were performed using Prism 8 software (www.graphpad.com), and graphs were generated in Prism 9, IGOR Pro software, or MATLAB. For analyses on imaging experiments, n refers to the number of non-overlapping fields of view unless otherwise specified as previously reported by us and others [18,20,32]. For immunohistochemistry and rabies tracing experiments, n refers to the number of mice; for electrophysiological experiments, n refers to the number of neurons recorded. The n for each experiment is indicated in the figure legend in the first quantification panel for the particular comparison. Normality tests were first performed to determine if data sets were normally distributed. We carried out outlier analyses for all quantifications. Outlier analysis was performed for all data sets, and if found, statistical tests were performed a second time excluding these outliers. Exclusion of outliers did not change the outcome of the statistical analysis in any cases. Because the outlier data points represent biological variability and were not associated with experimental errors, we included them in the final analyses. The sample sizes used in this study were comparable to previous publications [18,20,32,89,113,114]. For data sets that follow normal distribution, statistical significance was determined using Student's t-tests (t-test), (indicated on graphs with asterisks, $*p < 0.05$; $**p < 0.01$; $***p < 0.001$, $****p < 0.0001$; ns, $p > 0.05$) ANOVA or two-way ANOVA (indicated by p values in legends as well as results). For multiple comparisons tests following ANOVA, multiplicity adjusted p values were reported (indicated on graphs with asterisks, $*p < 0.05$; $**p < 0.01$, $***p < 0.001$, $****p < 0.0001$; ns, $p > 0.05$). For data involving proportions as dependent variables, the arcsine-square-root transformation was first performed before ANOVA analysis. For data sets that did not have normal distributions or were too small to merit a normality test, Mann-Whitney test was used. Significance was based on p values < 0.05. Means and standard errors were reported for all results unless otherwise specified.

Data available upon request.

Supplementary Material

Refer to Web version on PubMed Central for supplementary material.

Acknowledgements:

We are grateful to A. Iannone, M. Ross, A. Joyner, S. Shi, D. Pisapia, and A. Rajadhyaksha for helpful discussions. In addition, we recognize the generosity of the Genetically-Encoded Neuronal Indicator and Effector (GENIE) Project and the Janelia Research Campus for making GCaMP6s available. We are grateful to Georgiy Yudinstev and Robin Zhang for help with image collection and analysis.

Funding:

This work was supported by grants from NIH (NIMH 5R01MH110553, NINDS 1R01NS116137), Brain Research Foundation Seed Grant, Irma Hirschl/Monique Weill-Caulier Career Scientist and Frueauff Foundation Awards to N.V.D.M.; from NIMH (1R01MH109685, 1R01MH118451) to C.L. Additional support for R.B. was provided by NIMH: 5F30MH117939; support for A.C. was provided by NARSAD Young Investigator Grant and NINDS: 1K99NS114166; support for R.N.F. by NIMH: 5F30MH115622; and support for Z.S.D., R.B., and R.N.F. by T32GM007739 from NIGMS to the Weill Cornell/Rockefeller/Sloan Kettering Tri-Institutional MD-PhD Program.

References and Notes:

1. Rubenstein JL, and Merzenich MM (2003). Model of autism: increased ratio of excitation/inhibition in key neural systems. Genes Brain Behav 2, 255–267. 10.1034/j.1601-183x.2003.00037.x. [PubMed: 14606691]
2. Chao HT, Chen H, Samaco RC, Xue M, Chahrour M, Yoo J, Neul JL, Gong S, Lu HC, Heintz N, et al. (2010). Dysfunction in GABA signalling mediates autism-like stereotypies and Rett syndrome phenotypes. Nature 468, 263–269. 10.1038/nature09582. [PubMed: 21068835]
3. Frohlich J, Miller MT, Bird LM, Garces P, Purtell H, Hoener MC, Philpot BD, Sidorov MS, Tan WH, Hernandez MC, et al. (2019). Electrophysiological Phenotype in Angelman Syndrome Differs Between Genotypes. Biol Psychiatry 85, 752–759. 10.1016/j.biopsych.2019.01.008. [PubMed: 30826071]
4. Parikshak NN, Luo R, Zhang A, Won H, Lowe JK, Chandran V, Horvath S, and Geschwind DH (2013). Integrative functional genomic analyses implicate specific molecular pathways and circuits in autism. Cell 155, 1008–1021. 10.1016/j.cell.2013.10.031. [PubMed: 24267887]
5. Sanders SJ, He X, Willsey AJ, Ercan-Sencicek AG, Samocha KE, Cicek AE, Murtha MT, Bal VH, Bishop SL, Dong S, et al. (2015). Insights into Autism Spectrum Disorder Genomic Architecture and Biology from 71 Risk Loci. Neuron 87, 1215–1233. 10.1016/j.neuron.2015.09.016. [PubMed: 26402605]
6. Satterstrom FK, Kosmicki JA, Wang J, Breen MS, De Rubeis S, An JY, Peng M, Collins R, Grove J, Klei L, et al. (2020). Large-Scale Exome Sequencing Study Implicates Both Developmental and Functional Changes in the Neurobiology of Autism. Cell 180, 568–584 e523. 10.1016/j.cell.2019.12.036. [PubMed: 31981491]
7. Laurie DJ, Wisden W, and Seeburg PH (1992). The distribution of thirteen GABAA receptor subunit mRNAs in the rat brain. III. Embryonic and postnatal development. J Neurosci 12, 4151–4172. [PubMed: 1331359]
8. Cao J, O'Day DR, Pliner HA, Kingsley PD, Deng M, Daza RM, Zager MA, Aldinger KA, Blecher-Gonen R, Zhang F, et al. (2020). A human cell atlas of fetal gene expression. Science 370. 10.1126/science.aba7721.
9. AllenBrainAtlas (2020a). Brainspan: Atlas of the developing human brain. https://www.brainspan.org/rnaseq/searches?search_type=user_selections.
10. AllenBrainAtlas (2020b). Transcriptomic Explorer. https://celltypes.brain-map.org/rnaseq/mouse_ctx-hpf_10x?selectedVisualization=Heatmap&colorByFeature=Cell+Type&colorByFeatureValue=Gad1.
11. AllenBrainAtlas (2020c). Mouse Brain Atlas. https://mouse.brain-map.org/experiment/thumbnails/100048576?image_type=atlas.
12. Wolff JJ, Gerig G, Lewis JD, Soda T, Styner MA, Vachet C, Botteron KN, Elison JT, Dager SR, Estes AM, et al. (2015). Altered corpus callosum morphology associated with autism over the first 2 years of life. Brain 138, 2046–2058. 10.1093/brain/awv118. [PubMed: 25937563]

13. Rodriguez-Garcia ME, Cotrina-Vinagre FJ, Gomez-Cano MLA, Martinez de Aragon A, Martin-Hernandez E, and Martinez-Azorin F (2020). MAST1 variant causes mega-corpus-callosum syndrome with cortical malformations but without cerebellar hypoplasia. Am J Med Genet A 182, 1483–1490. 10.1002/ajmg.a.61560. [PubMed: 32198973]

14. Fenlon LR, Suarez R, and Richards LJ (2017). The anatomy, organisation and development of contralateral callosal projections of the mouse somatosensory cortex. Brain Neurosci Adv 1, 2398212817694888. 10.1177/2398212817694888. [PubMed: 32166131]

15. Fame RM, MacDonald JL, and Macklis JD (2011). Development, specification, and diversity of callosal projection neurons. Trends Neurosci 34, 41–50. 10.1016/j.tins.2010.10.002. [PubMed: 21129791]

16. Yamashita T, Vavladeli A, Pala A, Galan K, Crochet S, Petersen SSA, and Petersen CCH (2018). Diverse Long-Range Axonal Projections of Excitatory Layer 2/3 Neurons in Mouse Barrel Cortex. Front Neuroanat 12, 33. 10.3389/fnana.2018.00033. [PubMed: 29765308]

17. Zakiewicz IM, Bjaalie JG, and Leergaard TB (2014). Brain-wide map of efferent projections from rat barrel cortex. Front Neuroinform 8, 5. 10.3389/fninf.2014.00005. [PubMed: 24550819]

18. Duan ZRS, Che A, Chu P, Modol L, Bollmann Y, Babij R, Fetcho RN, Otsuka T, Fuccillo MV, Liston C, et al. (2020). GABAergic Restriction of Network Dynamics Regulates Interneuron Survival in the Developing Cortex. Neuron 105, 75–92 e75. 10.1016/j.neuron.2019.10.008. [PubMed: 31780329]

19. Golshani P, Goncalves JT, Khoshkhoo S, Mostany R, Smirnakis S, and Portera-Cailliau C (2009). Internally mediated developmental desynchronization of neocortical network activity. J Neurosci 29, 10890–10899. 10.1523/JNEUROSCI.2012-09.2009. [PubMed: 19726647]

20. Che A, Babij R, Iannone AF, Fetcho RN, Ferrer M, Liston C, Fishell G, and De Marco Garcia NV (2018). Layer I Interneurons Sharpen Sensory Maps during Neonatal Development. Neuron 99, 98–116 e117. 10.1016/j.neuron.2018.06.002. [PubMed: 29937280]

21. Kalemaki K, Velli A, Christodoulou O, Denaxa M, Karagogeos D, and Sidiropoulou K (2022). The developmental changes in intrinsic and synaptic properties of prefrontal neurons enhance local network activity from the second to the third postnatal weeks in mice. Cereb Cortex 32, 3633–3650. 10.1093/cercor/bhab438. [PubMed: 34905772]

22. De Felipe J, Marco P, Fairen A, and Jones EG (1997). Inhibitory synaptogenesis in mouse somatosensory cortex. Cereb Cortex 7, 619–634. 10.1093/cercor/7.7.619. [PubMed: 9373018]

23. Wamsley B, Jaglin XH, Favuzzi E, Quattrocolo G, Nigro MJ, Yusuf N, Khodadadi-Jamayran A, Rudy B, and Fishell G (2018). Rbfox1 Mediates Cell-type-Specific Splicing in Cortical Interneurons. Neuron 100, 846–859 e847. 10.1016/j.neuron.2018.09.026. [PubMed: 30318414]

24. Kaeser PS, and Regehr WG (2014). Molecular mechanisms for synchronous, asynchronous, and spontaneous neurotransmitter release. Annu Rev Physiol 76, 333–363. 10.1146/annurev-physiol-021113-170338. [PubMed: 24274737]

25. Nguyen QA, and Nicoll RA (2018). The GABAA Receptor beta Subunit Is Required for Inhibitory Transmission. Neuron 98, 718–725 e713. 10.1016/j.neuron.2018.03.046. [PubMed: 29706582]

26. Ramadan E, Fu Z, Losi G, Homanics GE, Neale JH, and Vicini S (2003). GABA(A) receptor beta3 subunit deletion decreases alpha2/3 subunits and IPSC duration. J Neurophysiol 89, 128–134. 10.1152/jn.00700.2002. [PubMed: 12522165]

27. Huntsman MM, Porcello DM, Homanics GE, DeLorey TM, and Huguenard JR (1999). Reciprocal inhibitory connections and network synchrony in the mammalian thalamus. Science 283, 541–543. 10.1126/science.283.5401.541. [PubMed: 9915702]

28. De Marco Garcia NV, Priya R, Tuncdemir SN, Fishell G, and Karayannis T (2015). Sensory inputs control the integration of neurogliaform interneurons into cortical circuits. Nat Neurosci 18, 393–401. 10.1038/nn.3946. [PubMed: 25664912]

29. Hand RA, Khalid S, Tam E, and Kolodkin AL (2015). Axon Dynamics during Neocortical Laminar Innervation. Cell Rep 12, 172–182. 10.1016/j.celrep.2015.06.026. [PubMed: 26146079]

30. Ma H, Harris S, Rahmani R, Lacefield CO, Zhao M, Daniel AG, Zhou Z, Bruno RM, Berwick J, and Schwartz TH (2014). Wide-field in vivo neocortical calcium dye imaging using a convection-enhanced loading technique combined with simultaneous multiwavelength imaging of voltage-

sensitive dyes and hemodynamic signals. Neurophotonics 1, 015003. 10.1117/1.NPh.1.1.015003. [PubMed: 25525611]

31. Akhmetshina D, Nasretdinov A, Zakharov A, Valeeva G, and Khazipov R (2016). The Nature of the Sensory Input to the Neonatal Rat Barrel Cortex. J Neurosci 36, 9922–9932. 10.1523/JNEUROSCI.1781-16.2016. [PubMed: 27656029]
32. Modol L, Bollmann Y, Tressard T, Baude A, Che A, Duan ZRS, Babij R, De Marco Garcia NV, and Cossart R (2020). Assemblies of Perisomatic GABAergic Neurons in the Developing Barrel Cortex. Neuron 105, 93–105 e104. 10.1016/j.neuron.2019.10.007. [PubMed: 31780328]
33. Delahanty RJ, Kang JQ, Brune CW, Kistner EO, Courchesne E, Cox NJ, Cook EH Jr., Macdonald RL, and Sutcliffe JS (2011). Maternal transmission of a rare GABRB3 signal peptide variant is associated with autism. Mol Psychiatry 16, 86–96. 10.1038/mp.2009.118. [PubMed: 19935738]
34. Buxbaum JD, Silverman JM, Smith CJ, Greenberg DA, Kilifarski M, Reichert J, Cook EH Jr., Fang Y, Song CY, and Vitale R (2002). Association between a GABRB3 polymorphism and autism. Mol Psychiatry 7, 311–316. 10.1038/sj.mp.4001011. [PubMed: 11920158]
35. Hahamy A, Behrmann M, and Malach R (2015). The idiosyncratic brain: distortion of spontaneous connectivity patterns in autism spectrum disorder. Nat Neurosci 18, 302–309. 10.1038/nn.3919. [PubMed: 25599222]
36. Di Martino A, O'Connor D, Chen B, Alaerts K, Anderson JS, Assaf M, Balsters JH, Baxter L, Beggiato A, Bernaerts S, et al. (2017). Enhancing studies of the connectome in autism using the autism brain imaging data exchange II. Sci Data 4, 170010. 10.1038/sdata.2017.10. [PubMed: 28291247]
37. Di Martino A, Yan CG, Li Q, Denio E, Castellanos FX, Alaerts K, Anderson JS, Assaf M, Bookheimer SY, Dapretto M, et al. (2014). The autism brain imaging data exchange: towards a large-scale evaluation of the intrinsic brain architecture in autism. Mol Psychiatry 19, 659–667. 10.1038/mp.2013.78. [PubMed: 23774715]
38. Hawrylycz M, Miller JA, Menon V, Feng D, Dolbeare T, Guillozet-Bongaarts AL, Jegga AG, Aronow BJ, Lee CK, Bernard A, et al. (2015). Canonical genetic signatures of the adult human brain. Nat Neurosci 18, 1832–1844. 10.1038/nn.4171. [PubMed: 26571460]
39. Hawrylycz MJ, Lein ES, Guillozet-Bongaarts AL, Shen EH, Ng L, Miller JA, van de Lagemaat LN, Smith KA, Ebbert A, Riley ZL, et al. (2012). An anatomically comprehensive atlas of the adult human brain transcriptome. Nature 489, 391–399. 10.1038/nature11405. [PubMed: 22996553]
40. Basu SN, Kollu R, and Banerjee-Basu S (2009). AutDB: a gene reference resource for autism research. Nucleic Acids Res 37, D832–836. 10.1093/nar/gkn835. [PubMed: 19015121]
41. Mizuno H, Hirano T, and Tagawa Y (2010). Pre-synaptic and post-synaptic neuronal activity supports the axon development of callosal projection neurons during different post-natal periods in the mouse cerebral cortex. Eur J Neurosci 31, 410–424. 10.1111/j.1460-9568.2009.07070.x. [PubMed: 20105242]
42. Suarez R, Fenlon LR, Marek R, Avitan L, Sah P, Goodhill GJ, and Richards LJ (2014). Balanced interhemispheric cortical activity is required for correct targeting of the corpus callosum. Neuron 82, 1289–1298. 10.1016/j.neuron.2014.04.040. [PubMed: 24945772]
43. Wang CL, Zhang L, Zhou Y, Zhou J, Yang XJ, Duan SM, Xiong ZQ, and Ding YQ (2007). Activity-dependent development of callosal projections in the somatosensory cortex. J Neurosci 27, 11334–11342. 10.1523/JNEUROSCI.3380-07.2007. [PubMed: 17942728]
44. Mojtahedi N, Kovalchuk Y, Bottcher A, and Garaschuk O (2021). Stable behavioral state-specific large scale activity patterns in the developing cortex of neonates. Cell Calcium 98, 102448. 10.1016/j.ceca.2021.102448. [PubMed: 34375923]
45. Wong FK, Bercsenyi K, Sreenivasan V, Portales A, Fernandez-Otero M, and Marin O (2018). Pyramidal cell regulation of interneuron survival sculpts cortical networks. Nature 557, 668–673. 10.1038/s41586-018-0139-6. [PubMed: 29849154]
46. Oh WC, Lutzu S, Castillo PE, and Kwon HB (2016). De novo synaptogenesis induced by GABA in the developing mouse cortex. Science 353, 1037–1040. 10.1126/science.aaf5206. [PubMed: 27516412]

47. De Leon Reyes NS, Mederos S, Varela I, Weiss LA, Perea G, Galazo MJ, and Nieto M (2019). Transient callosal projections of L4 neurons are eliminated for the acquisition of local connectivity. Nat Commun 10, 4549. 10.1038/s41467-019-12495-w. [PubMed: 31591398]
48. Munz M, Gobert D, Schohl A, Poquerusse J, Podgorski K, Spratt P, and Ruthazer ES (2014). Rapid Hebbian axonal remodeling mediated by visual stimulation. Science 344, 904–909. 10.1126/science.1251593. [PubMed: 24855269]
49. Chen JL, Margolis DJ, Stankov A, Sumanovski LT, Schneider BL, and Helmchen F (2015). Pathway-specific reorganization of projection neurons in somatosensory cortex during learning. Nat Neurosci 18, 1101–1108. 10.1038/nn.4046. [PubMed: 26098757]
50. Klingler E, De la Rossa A, Fievre S, Devaraju K, Abe P, and Jabaudon D (2019). A Translaminar Genetic Logic for the Circuit Identity of Intracortically Projecting Neurons. Curr Biol 29, 332–339 e335. 10.1016/j.cub.2018.11.071. [PubMed: 30639110]
51. Mitchell BD, and Macklis JD (2005). Large-scale maintenance of dual projections by callosal and frontal cortical projection neurons in adult mice. J Comp Neurol 482, 17–32. 10.1002/cne.20428. [PubMed: 15612019]
52. Masse IO, Ross S, Bronchti G, and Boire D (2017). Asymmetric Direct Reciprocal Connections Between Primary Visual and Somatosensory Cortices of the Mouse. Cereb Cortex 27, 4361–4378. 10.1093/cercor/bhw239. [PubMed: 27522075]
53. Bieler M, Xu X, Marquardt A, and Hanganu-Opatz IL (2018). Multisensory integration in rodent tactile but not visual thalamus. Sci Rep 8, 15684. 10.1038/s41598-018-33815-y. [PubMed: 30356135]
54. Tavassoli T, Auyeung B, Murphy LC, Baron-Cohen S, and Chakrabarti B (2012). Variation in the autism candidate gene GABRB3 modulates tactile sensitivity in typically developing children. Mol Autism 3, 6. 10.1186/2040-2392-3-6. [PubMed: 22769427]
55. DeLorey TM, Sahbaie P, Hashemi E, Li WW, Salehi A, and Clark DJ (2011). Somatosensory and sensorimotor consequences associated with the heterozygous disruption of the autism candidate gene, Gabrb3. Behav Brain Res 216, 36–45. 10.1016/j.bbr.2010.06.032. [PubMed: 20699105]
56. Orefice LL, Zimmerman AL, Chirila AM, Sleboda SJ, Head JP, and Ginty DD (2016). Peripheral Mechanosensory Neuron Dysfunction Underlies Tactile and Behavioral Deficits in Mouse Models of ASDs. Cell 166, 299–313. 10.1016/j.cell.2016.05.033. [PubMed: 27293187]
57. Samaco RC, Hogart A, and LaSalle JM (2005). Epigenetic overlap in autism-spectrum neurodevelopmental disorders: MECP2 deficiency causes reduced expression of UBE3A and GABRB3. Hum Mol Genet 14, 483–492. 10.1093/hmg/ddi045. [PubMed: 15615769]
58. Fatemi SH, Folsom TD, Kneeland RE, and Liesch SB (2011). Metabotropic glutamate receptor 5 upregulation in children with autism is associated with underexpression of both Fragile X mental retardation protein and GABAA receptor beta 3 in adults with autism. Anat Rec (Hoboken) 294, 1635–1645. 10.1002/ar.21299. [PubMed: 21901840]
59. Cheyne JE, Zabouri N, Baddeley D, and Lohmann C (2019). Spontaneous Activity Patterns Are Altered in the Developing Visual Cortex of the Fmr1 Knockout Mouse. Front Neural Circuits 13, 57. 10.3389/fncir.2019.00057. [PubMed: 31616256]
60. Goncalves JT, Anstey JE, Golshani P, and Portera-Cailliau C (2013). Circuit level defects in the developing neocortex of Fragile X mice. Nat Neurosci 16, 903–909. 10.1038/nn.3415. [PubMed: 23727819]
61. Lee LJ, Tsytsarev V, and Erzurumlu RS (2017). Structural and functional differences in the barrel cortex of Mecp2 null mice. J Comp Neurol 525, 3951–3961. 10.1002/cne.24315. [PubMed: 28857161]
62. He CX, Cantu DA, Mantri SS, Zeiger WA, Goel A, and Portera-Cailliau C (2017). Tactile Defensiveness and Impaired Adaptation of Neuronal Activity in the Fmr1 Knock-Out Mouse Model of Autism. J Neurosci 37, 6475–6487. 10.1523/JNEUROSCI.0651-17.2017. [PubMed: 28607173]
63. Bitzenhofer SH, Popplau JA, Chini M, Marquardt A, and Hanganu-Opatz IL (2021). A transient developmental increase in prefrontal activity alters network maturation and causes cognitive dysfunction in adult mice. Neuron 109, 1350–1364 e1356. 10.1016/j.neuron.2021.02.011. [PubMed: 33675685]

64. Pavone P, Pappalardo XG, Marino SD, Sciuto L, Corsello G, Ruggieri M, Parano E, Piccione M, and Falsaperla R (2020). A novel GABRB3 variant in Dravet syndrome: Case report and literature review. Mol Genet Genomic Med 8, e1461. 10.1002/mgg3.1461. [PubMed: 32945607]

65. Ferguson C, Hardy SL, Werner DF, Hileman SM, Delorey TM, and Homanics GE (2007). New insight into the role of the beta3 subunit of the GABAA-R in development, behavior, body weight regulation, and anesthesia revealed by conditional gene knockout. BMC Neurosci 8, 85. 10.1186/1471-2202-8-85. [PubMed: 17927825]

66. Homanics GE, DeLorey TM, Firestone LL, Quinlan JJ, Handforth A, Harrison NL, Krasowski MD, Rick CE, Korpi ER, Makela R, et al. (1997). Mice devoid of gamma-aminobutyrate type A receptor beta3 subunit have epilepsy, cleft palate, and hypersensitive behavior. Proc Natl Acad Sci U S A 94, 4143–4148. 10.1073/pnas.94.8.4143. [PubMed: 9108119]

67. Babb TL, Wilson CL, and Isokawa-Akesson M (1987). Firing patterns of human limbic neurons during stereoencephalography (SEEG) and clinical temporal lobe seizures. Electroencephalogr Clin Neurophysiol 66, 467–482. 10.1016/0013-4694(87)90093-9. [PubMed: 2438112]

68. Jiruska P, de Curtis M, Jefferys JG, Schevon CA, Schiff SJ, and Schindler K (2013). Synchronization and desynchronization in epilepsy: controversies and hypotheses. J Physiol 591, 787–797. 10.1113/jphysiol.2012.239590. [PubMed: 23184516]

69. Truccolo W, Donoghue JA, Hochberg LR, Eskandar EN, Madsen JR, Anderson WS, Brown EN, Halgren E, and Cash SS (2011). Single-neuron dynamics in human focal epilepsy. Nat Neurosci 14, 635–641. 10.1038/nn.2782. [PubMed: 21441925]

70. Dimidschstein J, Chen Q, Tremblay R, Rogers SL, Saldi GA, Guo L, Xu Q, Liu R, Lu C, Chu J, et al. (2016). A viral strategy for targeting and manipulating interneurons across vertebrate species. Nat Neurosci 19, 1743–1749. 10.1038/nn.4430. [PubMed: 27798629]

71. Matsuda T, and Cepko CL (2007). Controlled expression of transgenes introduced by in vivo electroporation. Proc Natl Acad Sci U S A 104, 1027–1032. 10.1073/pnas.0610155104. [PubMed: 17209010]

72. De Marco Garcia NV, Karayannis T, and Fishell G (2011). Neuronal activity is required for the development of specific cortical interneuron subtypes. Nature 472, 351–355. 10.1038/nature09865. [PubMed: 21460837]

73. Haubensak W, Kunwar PS, Cai H, Ciocchi S, Wall NR, Ponnusamy R, Biag J, Dong HW, Deisseroth K, Callaway EM, et al. (2010). Genetic dissection of an amygdala microcircuit that gates conditioned fear. Nature 468, 270–276. 10.1038/nature09553. [PubMed: 21068836]

74. Beier KT, Steinberg EE, DeLoach KE, Xie S, Miyamichi K, Schwarz L, Gao XJ, Kremer EJ, Malenka RC, and Luo L (2015). Circuit Architecture of VTA Dopamine Neurons Revealed by Systematic Input-Output Mapping. Cell 162, 622–634. 10.1016/j.cell.2015.07.015. [PubMed: 26232228]

75. Gorski JA, Talley T, Qiu M, Puelles L, Rubenstein JL, and Jones KR (2002). Cortical excitatory neurons and glia, but not GABAergic neurons, are produced in the Emx1-expressing lineage. J Neurosci 22, 6309–6314. 20026564. [PubMed: 12151506]

76. Loo L, Simon JM, Xing L, McCoy ES, Niehaus JK, Guo J, Anton ES, and Zylka MJ (2019). Single-cell transcriptomic analysis of mouse neocortical development. Nat Commun 10, 134. 10.1038/s41467-018-08079-9. [PubMed: 30635555]

77. Power JD, Cohen AL, Nelson SM, Wig GS, Barnes KA, Church JA, Vogel AC, Laumann TO, Miezin FM, Schlaggar BL, and Petersen SE (2011). Functional network organization of the human brain. Neuron 72, 665–678. 10.1016/j.neuron.2011.09.006. [PubMed: 22099467]

78. DeNardo LA, Berns DS, DeLoach K, and Luo L (2015). Connectivity of mouse somatosensory and prefrontal cortex examined with trans-synaptic tracing. Nat Neurosci 18, 1687–1697. 10.1038/nn.4131. [PubMed: 26457553]

79. Dzyubenko E, Fleischer M, Manrique-Castano D, Borbor M, Kleinschnitz C, Faissner A, and Hermann DM (2021). Inhibitory control in neuronal networks relies on the extracellular matrix integrity. Cell Mol Life Sci 78, 5647–5663. 10.1007/s00018-021-03861-3. [PubMed: 34128077]

80. Johnson MA, Contoreggi NH, Kogan JF, Bryson M, Rubin BR, Gray JD, Kreek MJ, McEwen BS, and Milner TA (2021). Chronic stress differentially alters mRNA expression of opioid peptides

and receptors in the dorsal hippocampus of female and male rats. J Comp Neurol 529, 2636–2657. 10.1002/cne.25115. [PubMed: 33483980]

81. Kersigo J, Pan N, Lederman JD, Chatterjee S, Abel T, Pavlinkova G, Silos-Santiago I, and Fritzsch B (2018). A RNAscope whole mount approach that can be combined with immunofluorescence to quantify differential distribution of mRNA. Cell Tissue Res 374, 251–262. 10.1007/s00441-018-2864-4. [PubMed: 29974252]
82. Rajasethupathy P, Sankaran S, Marshel JH, Kim CK, Ferenczi E, Lee SY, Berndt A, Ramakrishnan C, Jaffe A, Lo M, et al. (2015). Projections from neocortex mediate top-down control of memory retrieval. Nature 526, 653–659. 10.1038/nature15389. [PubMed: 26436451]
83. Fan JL, Rivera JA, Sun W, Peterson J, Haeberle H, Rubin S, and Ji N (2020). High-speed volumetric two-photon fluorescence imaging of neurovascular dynamics. Nat Commun 11, 6020. 10.1038/s41467-020-19851-1. [PubMed: 33243995]
84. Daigle TL, Madisen L, Hage TA, Valley MT, Knoblich U, Larsen RS, Takeno MM, Huang L, Gu H, Larsen R, et al. (2018). A Suite of Transgenic Driver and Reporter Mouse Lines with Enhanced Brain-Cell-Type Targeting and Functionality. Cell 174, 465–480 e422. 10.1016/j.cell.2018.06.035. [PubMed: 30007418]
85. Steinmetz NA, Buetfering C, Lecoq J, Lee CR, Peters AJ, Jacobs EAK, Coen P, Ollerenshaw DR, Valley MT, de Vries SEJ, et al. (2017). Aberrant Cortical Activity in Multiple GCaMP6-Expressing Transgenic Mouse Lines. eNeuro 4. 10.1523/ENEURO.0207-17.2017.
86. Babola TA, Li S, Gribizis A, Lee BJ, Issa JB, Wang HC, Crair MC, and Bergles DE (2018). Homeostatic Control of Spontaneous Activity in the Developing Auditory System. Neuron 99, 511–524 e515. 10.1016/j.neuron.2018.07.004. [PubMed: 30077356]
87. Barson D, Hamodi AS, Shen X, Lur G, Constable RT, Cardin JA, Crair MC, and Higley MJ (2020). Simultaneous mesoscopic and two-photon imaging of neuronal activity in cortical circuits. Nat Methods 17, 107–113. 10.1038/s41592-019-0625-2. [PubMed: 31686040]
88. Wang Y, Sanghvi M, Gribizis A, Zhang Y, Song L, Morley B, Barson DG, Santos-Sacchi J, Navaratnam D, and Crair M (2021). Efferent feedback controls bilateral auditory spontaneous activity. Nat Commun 12, 2449. 10.1038/s41467-021-22796-8. [PubMed: 33907194]
89. Ackman JB, Burbridge TJ, and Crair MC (2012). Retinal waves coordinate patterned activity throughout the developing visual system. Nature 490, 219–225. 10.1038/nature11529. [PubMed: 23060192]
90. Allene C, Cattani A, Ackman JB, Bonifazi P, Aniksztejn L, Ben-Ari Y, and Cossart R (2008). Sequential generation of two distinct synapse-driven network patterns in developing neocortex. J Neurosci 28, 12851–12863. 10.1523/JNEUROSCI.3733-08.2008. [PubMed: 19036979]
91. Crepel V, Aronov D, Jorquera I, Represa A, Ben-Ari Y, and Cossart R (2007). A parturition-associated nonsynaptic coherent activity pattern in the developing hippocampus. Neuron 54, 105–120. 10.1016/j.neuron.2007.03.007. [PubMed: 17408581]
92. Dombeck DA, Khabbaz AN, Collman F, Adelman TL, and Tank DW (2007). Imaging large-scale neural activity with cellular resolution in awake, mobile mice. Neuron 56, 43–57. 10.1016/j.neuron.2007.08.003. [PubMed: 17920014]
93. Molyneaux BJ, Arlotta P, Menezes JR, and Macklis JD (2007). Neuronal subtype specification in the cerebral cortex. Nat Rev Neurosci 8, 427–437. 10.1038/nrn2151. [PubMed: 17514196]
94. Paxinos G, Halliday GM, Watson C, Koutcherov Y, and Wang H (2007). Atlast of the Developing Mouse Brain: E17.5, P0, P6 (Elevsier Inc.).
95. Liou JY, Baird-Daniel E, Zhao M, Daniel A, Schevon CA, Ma H, and Schwartz TH (2019). Burst suppression uncovers rapid widespread alterations in network excitability caused by an acute seizure focus. Brain 142, 3045–3058. 10.1093/brain/awz246. [PubMed: 31436790]
96. Ming Q, Liou JY, Yang F, Li J, Chu C, Zhou Q, Wu D, Xu S, Luo P, Liang J, et al. (2020). Isoflurane-Induced Burst Suppression Is a Thalamus-Modulated, Focal-Onset Rhythm With Persistent Local Asynchrony and Variable Propagation Patterns in Rats. Front Syst Neurosci 14, 599781. 10.3389/fnsys.2020.599781. [PubMed: 33510621]
97. Zhao M, McGarry LM, Ma H, Harris S, Berwick J, Yuste R, and Schwartz TH (2015). Optical triggered seizures using a caged 4-Aminopyridine. Front Neurosci 9, 25. 10.3389/fnins.2015.00025. [PubMed: 25698919]

98. Yang F, Li J, Song Y, Zhao M, Niemeyer JE, Luo P, Li D, Lin W, Ma H, and Schwartz TH (2021). Mesoscopic Mapping of Ictal Neurovascular Coupling in Awake Behaving Mice Using Optical Spectroscopy and Genetically Encoded Calcium Indicators. Front Neurosci 15, 704834. 10.3389/fnins.2021.704834. [PubMed: 34366781]

99. Kramer RS, and Pearlstein RD (1979). Cerebral cortical microfluorometry at isosbestic wavelengths for correction of vascular artifact. Science 205, 693–696. 10.1126/science.223243. [PubMed: 223243]

100. Ma Y, Shaik MA, Kim SH, Kozberg MG, Thibodeaux DN, Zhao HT, Yu H, and Hillman EM (2016). Wide-field optical mapping of neural activity and brain haemodynamics: considerations and novel approaches. Philos Trans R Soc Lond B Biol Sci 371. 10.1098/rstb.2015.0360.

101. Kozberg MG, Ma Y, Shaik MA, Kim SH, and Hillman EM (2016). Rapid Postnatal Expansion of Neural Networks Occurs in an Environment of Altered Neurovascular and Neurometabolic Coupling. J Neurosci 36, 6704–6717. 10.1523/JNEUROSCI.2363-15.2016. [PubMed: 27335402]

102. Drysdale AT, Grosenick L, Downar J, Dunlop K, Mansouri F, Meng Y, Fetcho RN, Zebley B, Oathes DJ, Etkin A, et al. (2017). Resting-state connectivity biomarkers define neurophysiological subtypes of depression. Nat Med 23, 28–38. 10.1038/nm.4246. [PubMed: 27918562]

103. Power JD, Barnes KA, Snyder AZ, Schlaggar BL, and Petersen SE (2012). Spurious but systematic correlations in functional connectivity MRI networks arise from subject motion. Neuroimage 59, 2142–2154. 10.1016/j.neuroimage.2011.10.018. [PubMed: 22019881]

104. Yan CG, Craddock RC, Zuo XN, Zang YF, and Milham MP (2013). Standardizing the intrinsic brain: towards robust measurement of inter-individual variation in 1000 functional connectomes. Neuroimage 80, 246–262. 10.1016/j.neuroimage.2013.04.081. [PubMed: 23631983]

105. Cerliani L, Mennes M, Thomas RM, Di Martino A, Thioux M, and Keysers C (2015). Increased Functional Connectivity Between Subcortical and Cortical Resting-State Networks in Autism Spectrum Disorder. JAMA Psychiatry 72, 767–777. 10.1001/jamapsychiatry.2015.0101. [PubMed: 26061743]

106. Dickie EW, Ameis SH, Shahab S, Calarco N, Smith DE, Miranda D, Viviano JD, and Voineskos AN (2018). Personalized Intrinsic Network Topography Mapping and Functional Connectivity Deficits in Autism Spectrum Disorder. Biol Psychiatry 84, 278–286. 10.1016/j.biopsych.2018.02.1174. [PubMed: 29703592]

107. Nunes AS, Peatfield N, Vakorin V, and Doesburg SM (2019). Idiosyncratic organization of cortical networks in autism spectrum disorder. Neuroimage 190, 182–190. 10.1016/j.neuroimage.2018.01.022. [PubMed: 29355768]

108. Oldehinkel M, Mennes M, Marquand A, Charman T, Tillmann J, Ecker C, Dell'Acqua F, Brandeis D, Banaschewski T, Baumeister S, et al. (2019). Altered Connectivity Between Cerebellum, Visual, and Sensory-Motor Networks in Autism Spectrum Disorder: Results from the EU-AIMS Longitudinal European Autism Project. Biol Psychiatry Cogn Neurosci Neuroimaging 4, 260–270. 10.1016/j.bpsc.2018.11.010. [PubMed: 30711508]

109. Uddin LQ, Supekar K, Lynch CJ, Khouzam A, Phillips J, Feinstein C, Ryali S, and Menon V (2013). Salience network-based classification and prediction of symptom severity in children with autism. JAMA Psychiatry 70, 869–879. 10.1001/jamapsychiatry.2013.104. [PubMed: 23803651]

110. Xu J, Wang H, Zhang L, Xu Z, Li T, Zhou Z, Zhou Z, Gan Y, and Hu Q (2018). Both Hypo-Connectivity and Hyper-Connectivity of the Insular Subregions Associated With Severity in Children With Autism Spectrum Disorders. Front Neurosci 12, 234. 10.3389/fnins.2018.00234. [PubMed: 29695950]

111. Arnatkeviciute A, Fulcher BD, and Fornito A (2019). A practical guide to linking brain-wide gene expression and neuroimaging data. Neuroimage 189, 353–367. 10.1016/j.neuroimage.2019.01.011. [PubMed: 30648605]

112. Alexander-Bloch AF, Shou H, Liu S, Satterthwaite TD, Glahn DC, Shinohara RT, Vandekar SN, and Raznahan A (2018). On testing for spatial correspondence between maps of human brain structure and function. Neuroimage 178, 540–551. 10.1016/j.neuroimage.2018.05.070. [PubMed: 29860082]

113. Karnani MM, Jackson J, Ayzenshtat I, Hamzehei Sichani A, Manoocheri K, Kim S, and Yuste R (2016). Opening Holes in the Blanket of Inhibition: Localized Lateral Disinhibition by VIP Interneurons. J Neurosci 36, 3471–3480. 10.1523/JNEUROSCI.3646-15.2016. [PubMed: 27013676]

114. Kirmse K, Kummer M, Kovalchuk Y, Witte OW, Garaschuk O, and Holthoff K (2015). GABA depolarizes immature neurons and inhibits network activity in the neonatal neocortex in vivo. Nat Commun 6, 7750. 10.1038/ncomms8750. [PubMed: 26177896]

Highlights

- *Gabrb3* is necessary for cortical network desynchronization in murine S1
- GABAergic disruption results in enhanced contralateral but not ipsilateral connectivity
- *Gabrb3* ablation leads to increased whisker-dependent responses during mouse development
- Spatial pattern of human *GABRB3* expression correlates with atypical connectivity in ASD

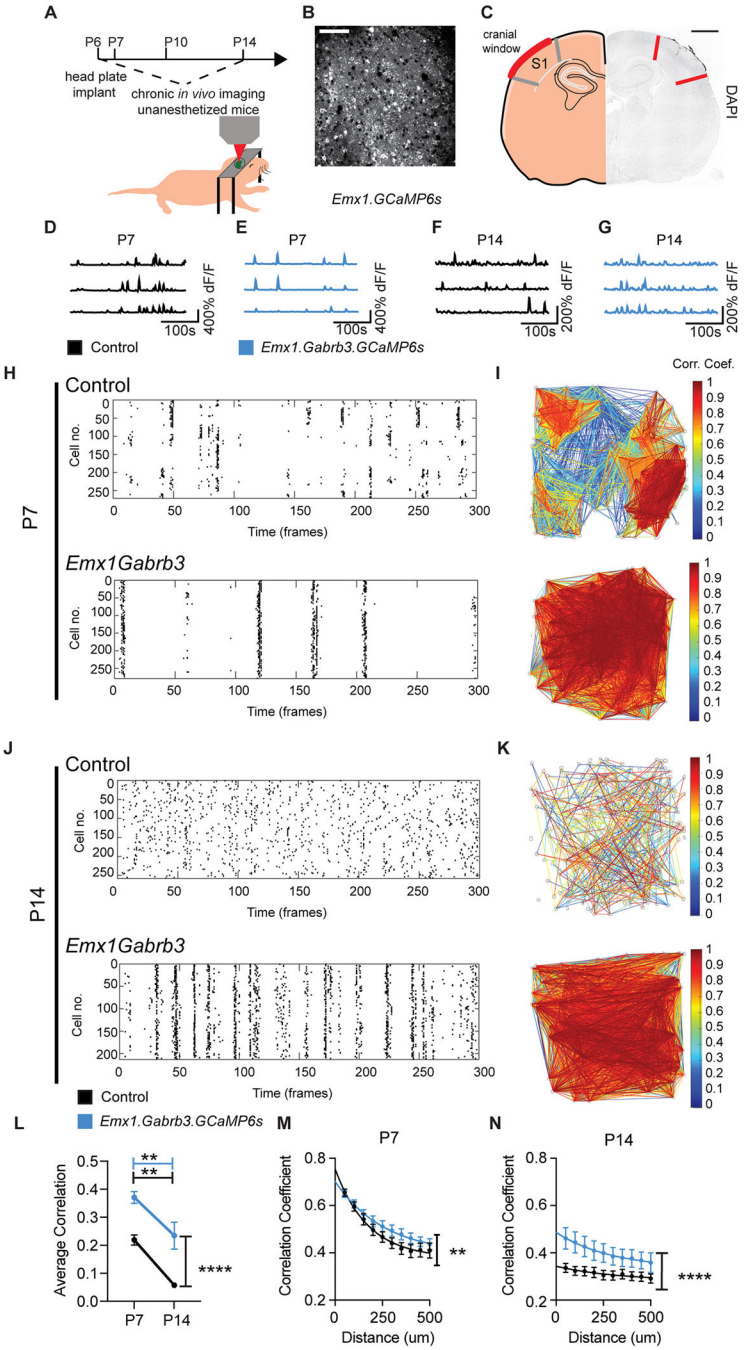

Figure 1. Long-lasting network synchronization after *Gabrb3* developmental deletion in cortical glutamatergic neurons.

A) Schematic representation of experimental procedures for the imaging of LII/III pyramidal neurons. P7: n=12 non-overlapping FOVs from 4 mice (control), 17 FOVs from 8 mice (*Emx1.Gabrb3*); P10: n=9 FOVs from 4 mice (control), 13 FOVs from 8 mice (*Emx1.Gabrb3*); P14: n=7 FOVs from 6 mice (control), 14 videos FOVs from 6 mice (*Emx1.Gabrb3*).

B) GCaMP6s expression in S1 pyramidal neurons of a P14 *Emx1.GCaMP6s* (control) mice. Scale bar = 100μm.

C) DAPI labeling delineates the location of the cranial window. Scale bar = 500μm.
D-G) Representative dF/F traces of 3 pyramidal neurons from *Emx1.GCaMP6s* mice at P7 (D) and P14 (F) and from *Emx1.Gabrb3.GCaMP6s* mice at P7 (E) and P14 (G).
H) Representative rastergram for calcium event onset in *Emx1.GCaMP6s* (top panel) and *Emx1.Gabrb3.GCaMP6s* (bottom panel) mice at P7.
I) Visualization of networks at P7 corresponding to recordings in (H): *Emx1.GCaMP6s* (top panel), *Emx1.Gabrb3.GCaMP6s* (bottom panel). Gray contours represent somas. Lines connect cell pairs exhibiting significantly correlated activity. Line color indicates the magnitude of the correlation coefficient.
J) Representative rastergram for calcium event onset in *Emx1.GCaMP6s* (top panel) and *Emx1.Gabrb3.GCaMP6s* (bottom panel) mice at P14.
K) Visualization of networks at P14 corresponding to recordings in (J): *Emx1.GCaMP6s* (top panel), *Emx1.Gabrb3.GCaMP6s* (bottom panel).
L) Quantification of the average correlation coefficient in *Emx1.GCaMP6s* (black) vs. *Emx1.Gabrb3.GCaMP6s* (blue) at P7 and P14. Two-way ANOVA for genotype ****p<0.0001 (Side asterisks); Sidak's multiple comparison: P7 **p=0.002, P14 **p=0.003. Two-way ANOVA for age ****p<0.0001; Sidak's multiple comparison: P7 vs. P14 control **p=0.009, *Emx1.Gabrb3* **p=0.003 (top asterisks).
M-N) Comparison of the correlation coefficient by distance in *Emx1.GCaMP6s* (black) vs. *Emx1.Gabrb3.GCaMP6s* (blue) at P7 (M) and P14 (N). Data per group fitted to an exponential decay function (solid lines), comparing the fit between control and mutants. Extra sum-of-squares F-test at P7 ** p=0.0026 and at P14 **** p<0.0001.
Data represent mean ± SEM.

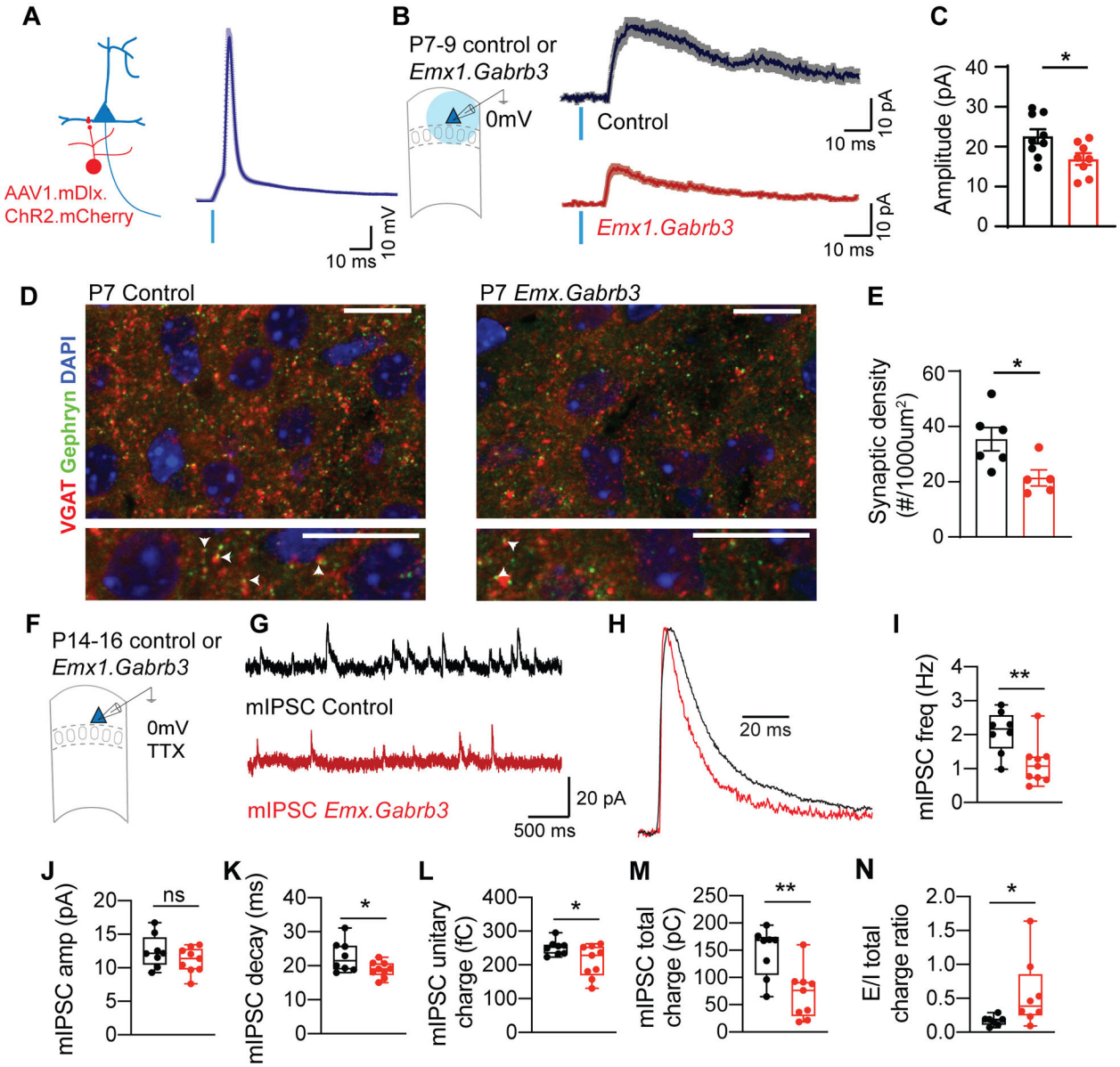

Figure 2. Early GABAergic dysfunction upon *Gabrb3* deletion in pyramidal neurons.

A-C) Optogenetic assessment of GABAergic function in control and *Emx.Gabrb3* mice at P7.

A) *AAV1.mDlx.ChR2.mCherry* expression in GABAergic interneurons mediates light-evoked action potentials in targeted recordings of interneurons expressing the virus (mCherry+) at P7.

B) Left: recording configuration of light-evoked IPSCs in layer II/III Pyr. Right: representative GABAergic currents in response to light stimulation in control (black) and *Emx.Gabrb3* (red) mice. The dark lines represent the average and the shaded area the SEM across multiple trials of stimulation. The blue line represents the onset and duration of optical stimulation.

C) Quantification of evoked IPSC amplitude. Control: n = 9 pyr; *Emx1.Gabrb3*: n = 8 pyr (t-test *p=0.026).
D-E) Anatomical characterization of GABAergic synapses in control and *Emx1.Gabrb3* mice at P7. Scale bars= 10μm.
D) Top: Representative image depicting immunolabeling for VGAT (red) and gephyrin (green) in L II/III of S1, DAPI in blue. Bottom: Higher magnification indicating putative GABAergic synapses delineated by the colocalization of VGAT and gephyrin puncta (arrowheads).
E) Quantification of GABAergic synaptic density per area. Control (6 mice) vs. *Emx1.Gabrb3* (5 mice); t-test *p=0.027.
F) Schematic representation of the recording configuration for mIPSCs (0 mV) in L II/III pyr in control and *Emx1.Gabrb3* mice at P14-16.
G) Sample traces of mIPSCs recorded in Pyr of control (black) and *Emx1.Gabrb3* mice (red).
H) Overlay of representative normalized average mIPSCs, corresponding to the traces in H).
I-M) mIPSC analysis summary. Control: n = 8 pyramidal neurons; *Emx1.Gabrb3*: n = 9 pyramidal neurons.
I) mIPSC frequency (t-test **p=0.007).
J) mIPSC amplitude (t-test ns).
K) mIPSC decay (t-test *p=0.042).
L) mIPSC unitary charge (t-test *p=0.045).
M) mIPSC total charge (t-test **p=0.003).
N) mEPSC/mIPSC total charge ratio. Control: n = 7 Pyr; Mutant: n = 8 Pyr. (Mann-Whitney test *p = 0.014).
Data represent mean ± SEM.

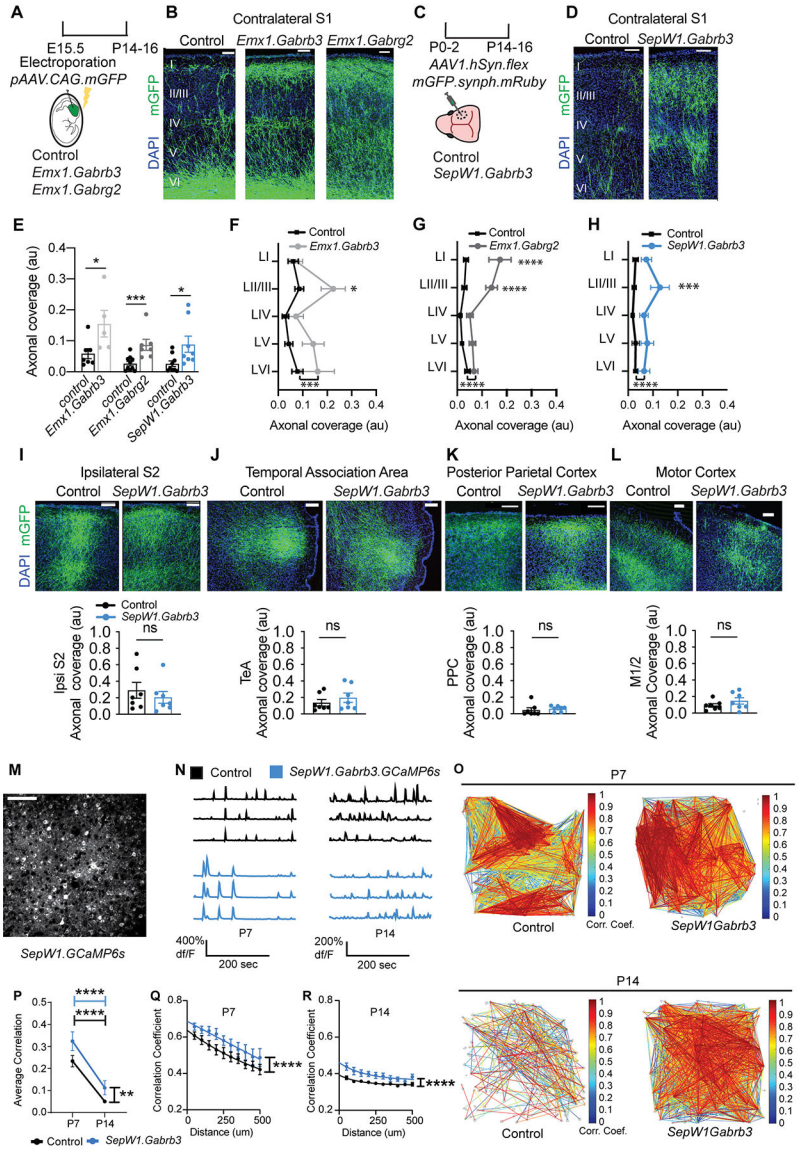

Figure 3. *SepW1.Gabrb3* mice show increased contralateral axonal coverage and correlated activity across postnatal development.

A) Schematic representation for the anatomical tracing of axonal terminals via *in utero* electroporation. *Emx1*^{Cre} or wild type (control), *Emx1.Gabrb3,* or *Emx1.Gabrg2* mice were electroporated at E15.5 with a *pAAV.CAG.mGFP* plasmid. Analysis of contralateral axonal arborization was performed at P14-16.

B) Representative images of axonal arborization in S1 contralateral to the electroporation site. Scale bar = 100μm; n=7 control, n=5 *Emx1.Gabrb3* mice; n=10 control, n=7 *Emx1.Gabrg2* mice.

C) Schematic representation for the anatomical tracing of axonal terminals via intracranial injections.

D) Representative images of axonal arborization in S1 contralateral to the injection site. Scale bar = 100μm; n=10 control vs. n=9 *SepW1.Gabrb3* mice.

E) Quantification of axonal coverage. Control vs *Emx1.Gabrb3:* Mann-Whitney test, *p=0.018. Control vs. *Emx1.Gabrg2*: Mann-Whitney test, ***p=0.0004. Control vs. *SepW1.Gabrb3*: Mann-Whitney test, *p=0.015. au, arbitrary units.

F-H) Axonal coverage by lamina. (F) Control vs. *Emx1.Gabrb3*: Two-way ANOVA for genotype ***p=0.0004, lamina p=0.01. Sidak's multiple comparison testing: LII/III *p=0.01, other lamina not significant. G) Axonal coverage by lamina. Control vs. *Emx1.Gabrg2*: Two-way ANOVA for genotype ****p<0.0001, lamina p<0.0001. Sidak's multiple comparison testing: LI, LII/III ****p<0.0001, other lamina not significant. H) Axonal coverage by lamina. Control vs. *SepW1.Gabrb3:* Two-way ANOVA for genotype ****p<0.0001. Sidak's multiple comparison testing: LII/III ***p=0.0009, other lamina not significant.

(I-L, top) Representative images (top) of axonal arborization in S1 target regions ipsilateral to viral injection site in control (left) and *SepW1.Gabrb3* (right) mice. Scale bars = 100μm.

(I-L, bottom) Quantification of normalized axonal coverage in ipsilateral S2 (I), temporal association area (TeA) (J), posterior parietal cortex (PPC) (K) and motor cortex (M1/2) (L). Mann-Whitney test, ns.

M) GCaMP6s expression in pyramidal neurons in S1 Pyr of a P14 *SepW1.GCaMP6s* (control) mice. Scale bar = 100μm.

N) Representative dF/F traces of 3 pyramidal neurons from *SepW1.GCaMP6s* mice at P7 (top left) and P14 (top right) and from *SepW1.Gabrb3.GCaMP6s* mice at P7 (bottom left) and P14 (bottom right).

O) Visualization of networks at P7 (top panels) and P14 (bottom panels) in *SepW1.GCaMP6s* (left panels), *SepW1.Gabrb3.GCaMP6s* (right panels).

P) Quantification of the average correlation coefficient in *SepW1.GCaMP6s* (black) vs. *SepW1.Gabrb3.GCaMP6s* (blue) at P7 and P14. Two-way ANOVA for genotype **p=0.006 (side asterisks) Sidak's multiple comparison: P7 p=0.06, P14 p=0.12. Two-way ANOVA for age **** p<0.0001 Sidak's multiple comparison: P7 vs. P14 Control ****p<0.0001, *SepW1.Gabrb3* ****p<0.0001 (top asterisks).

Q-R) Comparison of the correlation coefficient by distance in *SepW1.GCaMP6s* (black) vs. *SepW1.Gabrb3.GCaMP6s* (blue) at P7 (Q) and P14 (R). Data per group fitted to an exponential decay function (solid lines). Extra sum-of-squares F-test, both P7 and P14 **** p<0.0001. For panels P-R: *SepW1.GCaMP6s* at P7 (n=6 FOVs from 3 mice); P14 (n=10 FOVs from 3 mice) and *SepW1.Gabrb3.GCaMP6s* at P7 (n=5 FOVs from 2 mice); P14 (n=7 videos FOVs from 2 mice).

Data represent mean ± SEM.

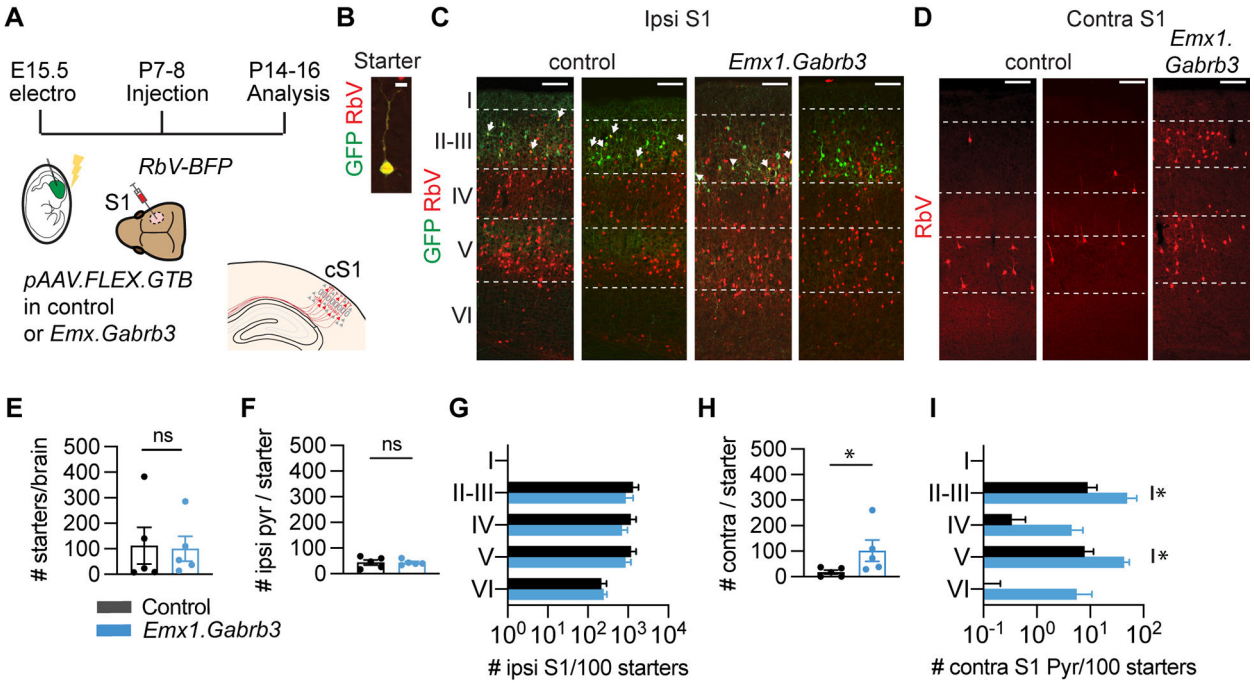

Figure 4. Selective increase of interhemispheric connectivity in *Emx1.Gabrb3* mice.

A) Schematic representation of experimental procedure used to trace afferent inputs onto pyramidal neurons (n=5 control mice, 5 *Emx1.Gabrb3* mice).

B) Starter neurons (right) co-express both BFP (RbV, pseudocolored in red) and GFP (electroporation construct).

C) Representative images of S1 ipsilateral to the electroporation and injection sites in *Emx1*^{Cre} (control, left two images) and *Emx1.Gabrb3* (right two images). Scale bar 100μm. Dotted lines indicate laminar boundaries.

D) Representative images of contralateral S1 in *Emx1*^{Cre} (control, left two images) and *Emx1.Gabrb3* mice (right). Scale bar 100μm.

E) Quantification of number of starter neurons per brain, Mann-Whitney test, ns.

F) Ratio of rabies-infected ipsilateral neurons over the total number of starter neurons, Mann-Whitney, ns.

G) Laminar distribution of rabies-infected neurons in ipsilateral S1. Two-way ANOVA, ns for genotype.

H) Ratio of rabies-infected contralateral neurons over the total of starter neurons, Mann-Whitney *p=0.03.

I) Laminar distribution of rabies-infected neurons in contralateral S1. Two-way ANOVA for genotype p=0.0036, for lamina p=0.0059. Sidak's post-hoc: LII/III *p=0.049, LV *p=0.02. Data represent mean ± SEM.

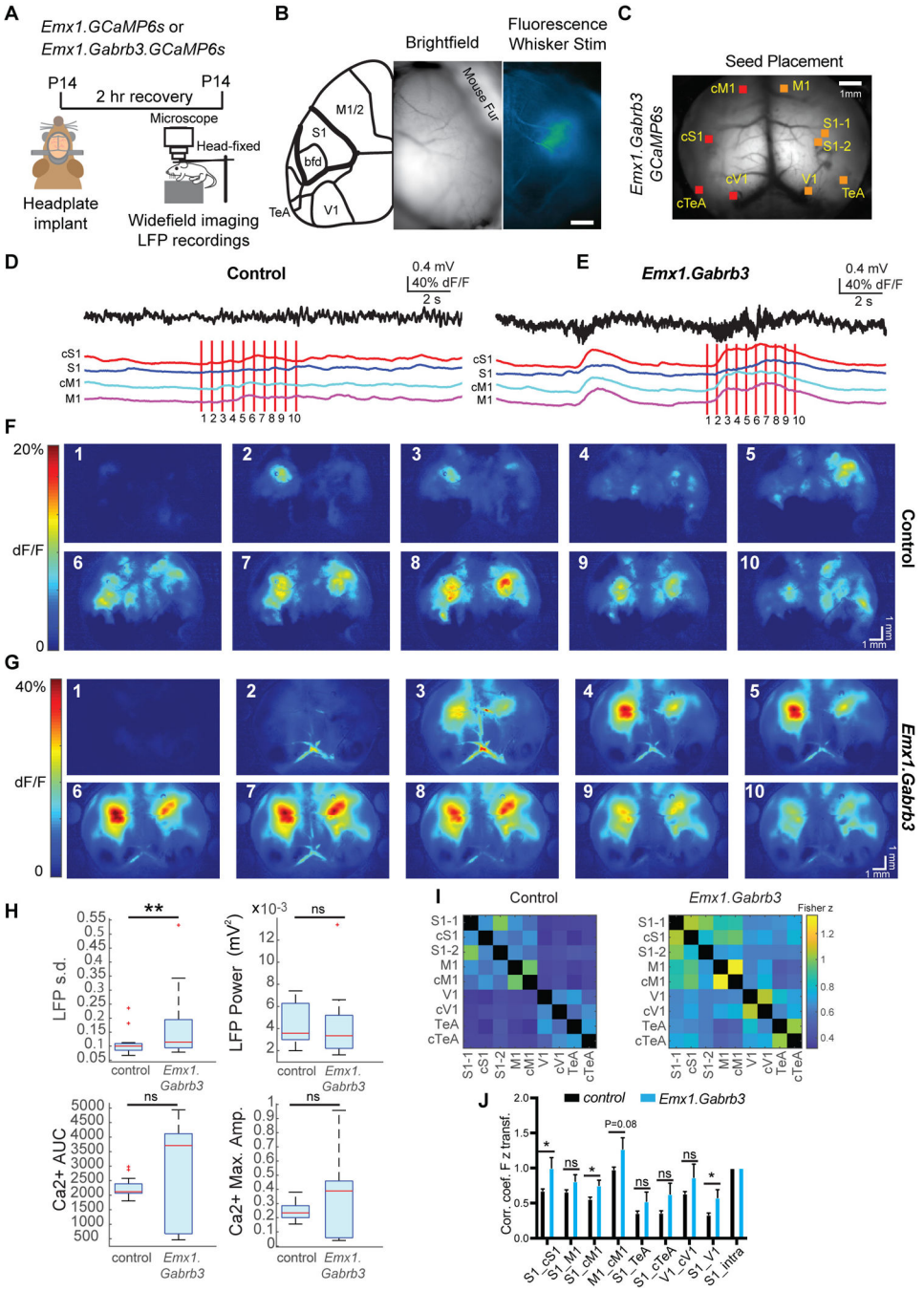

Figure 5. Increased functional contralateral connectivity in *Emx1.Gabrb3* mice.

A) Experimental procedure for widefield *in vivo* calcium at P14.

B) Map of dorsal cortical regions (left), and representative images of brightfield (middle) and calcium-mediated responses (right), taken during whisker stimulation to localize the barrel cortex. S1, primary somatosensory cortex; V1, primary visual cortex; bfd: barrel field; TeA, temporal association area; M1/2, motor cortex. Scale bar 1mm.

C) The placement of seed locations. Each seed covers an area of 0.2 X 0.2 mm^2.

D-E) Simultaneous recordings of LFP and calcium signal. LFP (top) and calcium traces (bottom) from 4 different locations in control (D) and *Emx1.Gabrb3* mice (E). Vertical red lines indicate the time points at which the 2D calcium image was generated.
F) 2D calcium activity during spontaneous activity. In control (F) (heatmap normalized to 20% dF/F) and *Emx1.Gabrb3* mice (G) (heatmap normalized to 40% dF/F).
H) Comparison of LFP and calcium activity in control (n=3) and mutant (n=2) mice. Top: boxplots of standard deviation (t-test, **p = 0.009) and power of LFP (t-test, p = 0.472). Bottom: area under curve (AUC) (t-test, p = 0.370) and maximal amplitude (t-test, p = 0.155) of calcium traces recorded from the ROI shown in C.
I-J) Global correlation of calcium activity.
I) Correlation matrix among different seeds in control and *Emx1.Gabrb3* mice.
J) Correlation in selected seed pairs between control and mutant mice. (t-test, $n_{control}$ = 29 sections from 3 mice, n_{mutant}= 27 sections from 2 mice, *: p<0.05). The Spearman correlation between different seeds was transformed into a Z-score by Fisher z-transformation and normalized to the intra-S1 Z-score.
Data represent mean ± SEM.

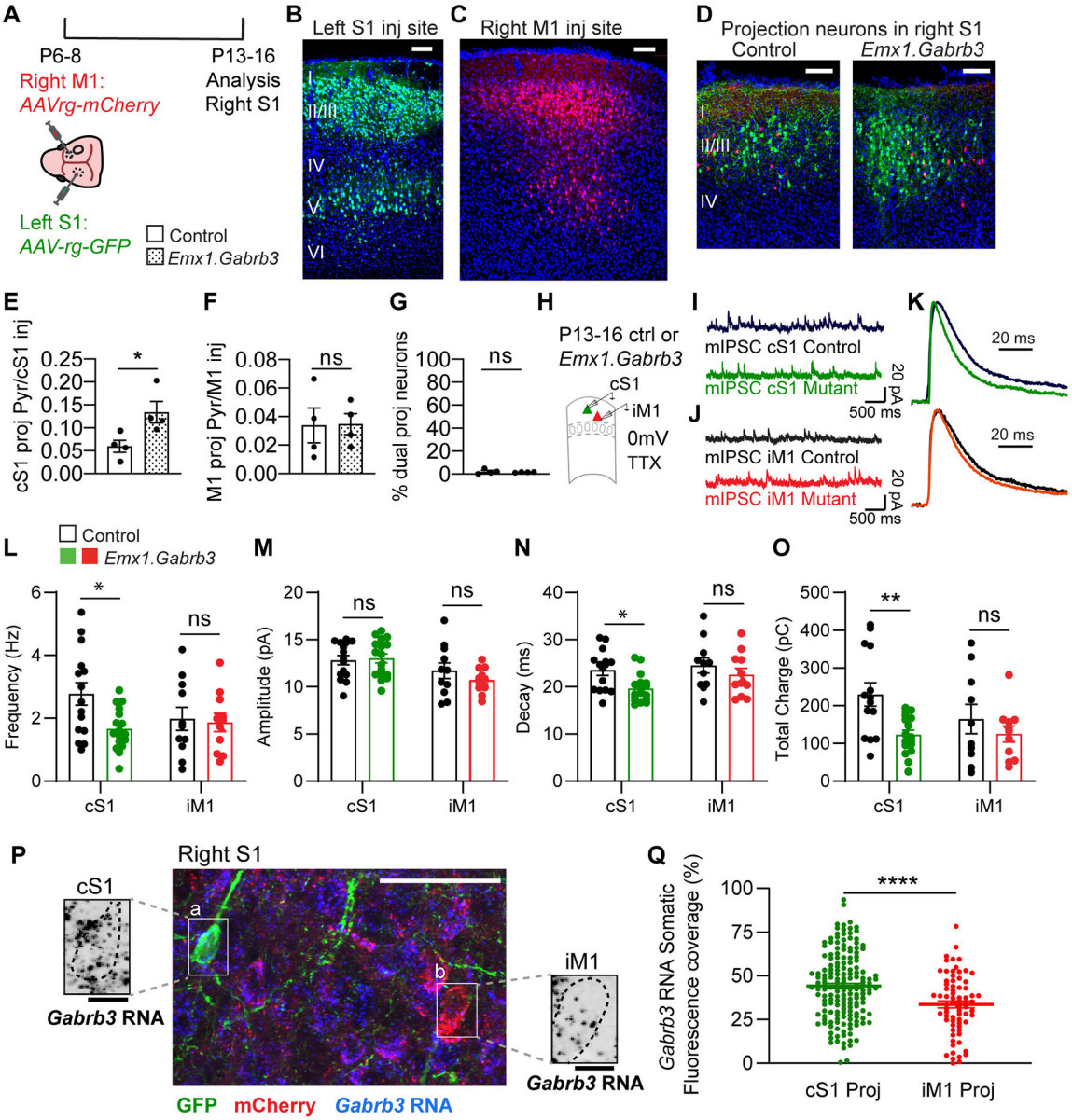

Figure 6. *Gabrb3* is highly expressed in contralaterally projecting pyramidal cells and is necessary for inhibitory synaptic function

A) Schematic representation for the identification of projection neurons as defined by their targets (n=4 control mice; n=4 *Emx1.Gabrb3* mice).

B-C) Representative images of the injection site in left S1 (B) and right M1 (C). Scale bar = 100μm.

D) Representative images of presynaptic cells in right S1 in control (left) and *Emx1.Gabrb3* (right) mice. Scale bar = 100μm.

E) Normalized number of contralaterally projecting neurons (cS1-projecting). Mann-Whitney test, *p=0.029.

F) Normalized number of ipsilateral M1-projecting neurons. Mann-Whitney test, ns.

G) Percentage of neurons in right S1 that co-express both mCherry and GFP in controls (2.08%) and *Emx1.Gabrb3* mice (1.58%), Mann-Whitney test, ns.
H) Schematic representation for the recording of mIPSCs in layer II/III S1 Pyr projecting to contralateral S1 (cS1 projecting, in green) or ipsilateral M1 (iM1 projecting, in red) at P13-16.
I-J) Sample traces of mIPSCs recorded in cS1 (I) and iM1 (J) projecting neurons in control (black) and *Emx1.Gabrb3* mice (green/red).
K) Normalized average mIPSCs, corresponding to the traces in I-J. Top: cS1 projecting, bottom: M1 projecting.
L-O) Analysis for mIPSC recorded in cS1 projecting neurons (Control: n=15 neurons; *Emx1.Gabrb3*: n =17 neurons) and M1 projecting neurons (Control: n=11 neurons; *Emx1.Gabrb3*: n =11 neurons).
L) mIPSC frequency (two-way ANOVA genotype *p=0.045; cS1: control vs. *Emx1.Gabrb3*, Bonferroni multiple comparison *p=0.010; M1: control vs. *Emx1.Gabrb3*, Bonferroni multiple comparison ns).
M) mIPSC amplitude (two-way ANOVA genotype ns).
N) mIPSC decay (two-way ANOVA genotype *p=0.016; cS1: control vs. *Emx1.Gabrb3*, Bonferroni multiple comparison *p=0.025; M1: control vs. *Emx1.Gabrb3*, Bonferroni multiple comparison ns).
O) mIPSC total charge (two-way ANOVA genotype p=0.007; cS1: control vs. *Emx1.Gabrb3*, Bonferroni multiple comparison **p=0.004; M1: control vs. *Emx1.Gabrb3*, Bonferroni multiple comparison ns).
P) Representative image of RNA FISH against *Gabrb3* (blue) in cS1 (green) and iM1-projecting (red) neurons retrogradely labelled as in A), scale bar 50μm. Insets: high magnification images of *Gabrb3* RNA expression (black) in the isolated cS1(a) and iM1-projecting neurons (b) (white boxes), dotted line indicates the somatic perimeter, scale bar 10μm.
Q) Quantification of *Gabrb3* expression in cS1and M1-projecting neurons, as the % somatic coverage of the fluorescent RNA FISH signal. cS1 44.2±1.47 (n=168 Pyr) vs. M1 33.6±2.02 (n=72 Pyr), t-test ****p<0.0001.
Data represent mean ± SEM.

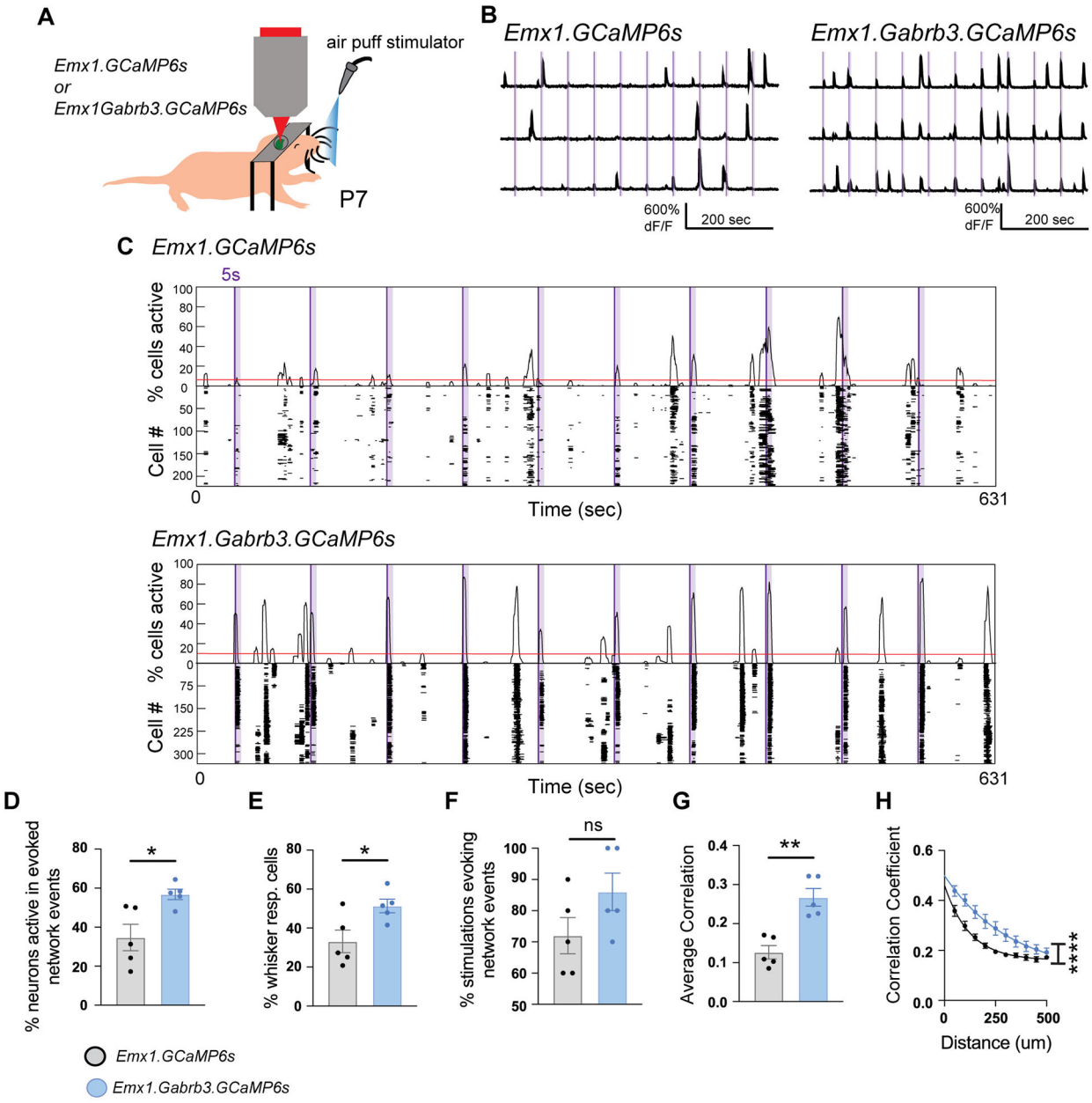

Figure 7. Increased whisker-evoked responses in *Emx1.Gabrb3* mice at P7.

A) Schematic representation for imaging of LII/III Pyr in whisker stimulation experiments at P7.

B) Three representative traces of single-cell calcium responses during whisker stimulation (purple vertical lines) in *Emx1.GCaMP6s* (left) and *Emx1.Gabrb3.GCaMP6s* (right) mice.

C) Representative event histograms and rastergrams for control *Emx1.GCaMP6s* (top) and *Emx1.Gabrb3.GCaMP6s* (bottom) mice. Dark purple vertical lines mark the onset of whisker stimulation (WS) by air puff and vertical purple shaded areas depict the time windows during which network events were quantified. Red horizontal lines indicate the threshold for network events. Each line in the rastergram represents a calcium event from onset to offset.

D) Percentage of neurons active in whisker-evoked network events. Control vs. *Emx1.Gabrb3*, t-test *p=0.016. (Control n=5 FOV from 3 mice; *Emx1.Gabrb3* n=5 FOV from 3 mice).
E) Percentage of whisker-responsive cells. Control vs. *Emx1.Gabrb3*, t-test *p=0.028.
F) Percentage of network events evoked by whisker stimulation. Control vs. *Emx1.Gabrb3*, t-test ns.
G) Quantification of the average correlation coefficient after whisker stimulation. Control vs. *Emx1.Gabrb3*, t-test **p=0.001.
H) Quantification of the average correlation over distance after whisker stimulation. Control vs. *Emx1.Gabrb3*, Extra sum-of-squares F-test ****p<0.0001.
Data represent mean ± SEM.

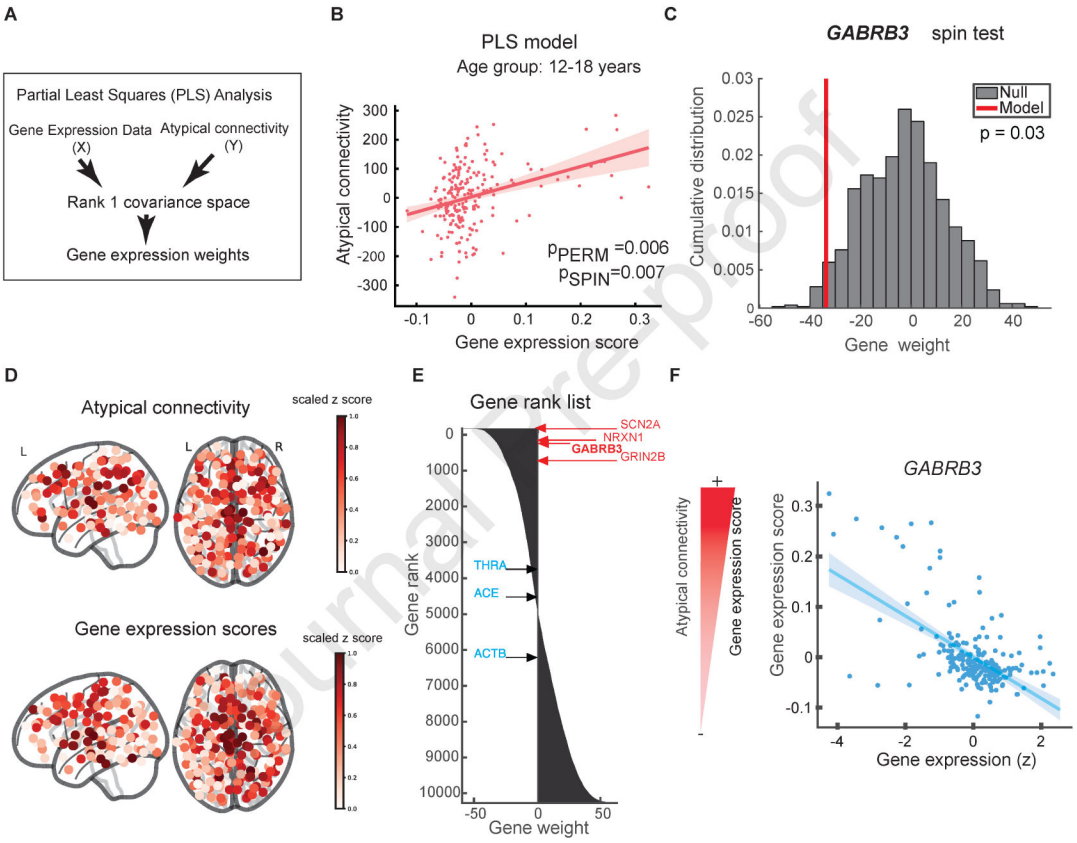

Figure 8. Variability in *Gabrb3* expression during adolescence underlies atypical functional connectivity in humans.

A) Overview of the PLS regression analysis to test for correlations between the AHBA dataset and atypical functional connectivity in ASD (ABIDE fMRI data set, ASD n= 261; 227 male, 34 female; ages 12–18, controls n= 235;187 male, 48 female; ages 12–18).

B) Scatterplot and linear fit defining the association between latent gene expression scores for the first PLS component from the PLS model (X axis) and atypical connectivity for the first PLS component (Y axis). Gene expression explained 12.1% of the variance in atypical connectivity (Y), and this was significantly more explained variance than expected by chance in both a shuffled spatially aware spin test (p=0.007) and a random permutation test (p=0.006).

C) Comparison of the bootstrapped gene weight for *GABRB3* expression with an empirical null distribution from PLS analysis (ages 12–18). *GABRB3* has a significantly stronger negative weight than expected by chance (p=0.03).

D) Glass brain maps depicting the spatial distribution of atypical connectivity (top) and gene expression score (bottom) across the 213 brain ROIs. Atypical connectivity and the gene expression Z scores were rescaled from 0–1 (see color bar).

E) Bar plot of the bootstrapped gene weight and rank for the first PLS component across all 10,438 genes from the age-restricted PLS analysis. High-risk ASD genes shown in red. Weakly associated ASD genes, shown in blue.

F) Scatterplot and linear fit of how well the normalized gene expression for *GABRB3* explained the latent gene expression score for the first PLS component across all ROIs. Decreased expression of *GABRB3* was correlated with increases in atypical connectivity.

KEY RESOURCES TABLE

REAGENT or RESOURCE	SOURCE	IDENTIFIER
Antibodies		
Goat polyclonal anti-GFP	Rockland	Cat# 600-101-215; RRID: AB_218182
Chicken polyclonal anti-RFP	Rockland	Cat# 600-901-379S, RRID:AB_10703148
Rat monoclonal anti-somatostatin	Millipore Sigma	Cat# MAB354, RRID:AB_2255365
Rabbit polyclonal anti-parvalbumin	Abcam	Cat# ab11427, RRID:AB_298032
Rabbit polyclonal anti-Satb2	Abcam	Cat# ab34735, RRID:AB_2301417
Rat monoclonal anti-Ctip2	Abcam	Cat# ab18465, RRID:AB_2064130
Streptavidin Pacific Blue	Thermo Fisher	Cat# S11222
Guinea pig monoclonal Anti-Gephyrin	Synaptic Systems	Cat# 147 318 RRID:AB_2661777
Rabbit polyclonal Anti-Vesicular GABA Transporter (VGAT)	Millipore Sigma	Cat# AB5062P RRID:AB_2301998
Bacterial and virus strains		
pAAV hSyn FLEx mGFP-2A-Synaptophysin-mRuby	Generated from UNC viral core from commercially available plasmid (see recombinant DNA)	
AAV1.Dlx1.ChR2.mCherry	Generated by Gordon Fishell[70]	Addgene Cat# 83898-AAV1
SAAG-RbV-BFP	Salk Institute	N/A
AVV.retrograde.hSyn.mCherry	Generated by Karl Deisseroth	Addgene Cat# 114472-AAVrg
AAV.retrograde.CAG.GFP	Generated by Edward Boyden	Addgene Cat# 37825-AAVrg
Chemicals, peptides, and recombinant proteins		
Tetrodotoxin Citrate	Abcam	Cat# ab120055
Critical commercial assays		
RNAScope Multiplex Fluorescent Assay	ACD	Cat# 323100
Experimental models: Organisms/strains		
$Gabrb3^{fl/fl}$	Jackson Labs	JAX 008310
$Emx1^{Cre}$	Jackson Labs	JAX 005628
Rosa.floxed.STOP.GCaMP6s (Ai96)	Jackson Labs	JAX 024106
$SepW1^{Cre}$	Sperm from GENSAT project	MGI NP-39
$Gabrg2^{fl/fl}$	Jackson Labs	JAX 003137
Oligonucleotides		
RNAScope Probe – Mm-Gabrb3	ACD	Cat# 492441
Recombinant DNA		
pAAV-CAG-mGFP	Generated by Connie Cepko[71]	Addgene Cat # 14757
pAAV-CAG-STOP-EGFP	Generated in house [72]	
pAAV-EF1a-FLEX-GTB	Generated by Edward Callaway[73]	Addgene Cat# 26197
pAAV hSyn FLEx mGFP-2A-Synaptophysin-mRuby	Generated by Liqun Luo[74]	Addgene Cat# 71760
Other		

REAGENT or RESOURCE	SOURCE	IDENTIFIER
ABIDE I-II dataset	http://fcon_1000.proiects.nitrc.ora/indi/abide/	
AHBA dataset	https://human.brain-map.org/static/download	